LETTER

https://doi.org/10.1038/s41586-018-0373-y

Unique features of mammalian mitochondrial translation initiation revealed by cryo–EM

Eva Kummer[1], Marc Leibundgut[1], Oliver Rackham[2], Richard G. Lee[2], Daniel Boehringer[1], Aleksandra Filipovska[2] & Nenad Ban[1]*

Mitochondria maintain their own specialized protein synthesis machinery, which in mammals is used exclusively for the synthesis of the membrane proteins responsible for oxidative phosphorylation[1,2]. The initiation of protein synthesis in mitochondria differs substantially from bacterial or cytosolic translation systems. Mitochondrial translation initiation lacks initiation factor 1, which is essential in all other translation systems from bacteria to mammals[3,4]. Furthermore, only one type of methionyl transfer RNA ($tRNA^{Met}$) is used for both initiation and elongation[4,5], necessitating that the initiation factor specifically recognizes the formylated version of $tRNA^{Met}$ ($fMet–tRNA^{Met}$). Lastly, most mitochondrial mRNAs do not possess 5′ leader sequences to promote mRNA binding to the ribosome[2]. There is currently little mechanistic insight into mammalian mitochondrial translation initiation, and it is not clear how mRNA engagement, initiator-tRNA recruitment and start-codon selection occur. Here we determine the cryo-EM structure of the complete translation initiation complex from mammalian mitochondria at 3.2 Å. We describe the function of an additional domain insertion that is present in the mammalian mitochondrial initiation factor 2 (mtIF2). By closing the decoding centre, this insertion stabilizes the binding of leaderless mRNAs and induces conformational changes in the rRNA nucleotides involved in decoding. We identify unique features of mtIF2 that are required for specific recognition of $fMet–tRNA^{Met}$ and regulation of its GTPase activity. Finally, we observe that the ribosomal tunnel in the initiating ribosome is blocked by insertion of the N-terminal portion of mitochondrial protein mL45, which becomes exposed as the ribosome switches to elongation mode and may have an additional role in targeting of mitochondrial ribosomes to the protein-conducting pore in the inner mitochondrial membrane.

We reconstituted the complete mammalian mitochondrial 55S translation initiation complex from purified porcine mitoribosomal subunits and purified recombinant human mtIF2, naturally occurring leaderless human *MT-CO3* mRNA and aminoacylated and formylated human $fMet–tRNA^{Met}$ stalled with a non-hydrolysable GTP analogue (GTPγS), and determined its structure at 3.2 Å resolution by cryo-electron microscopy (cryo-EM) (Fig. 1a, Extended Data Fig. 3). Using focused classification, we refined the cryo-EM maps to 3.2 Å and 3.1 Å for the 39S and the 28S subunits, respectively (Extended Data Fig. 2b), which enabled building and refinement of the atomic model (see Methods). The five major domains of mtIF2 are positioned to interact with the decoding centre in the A site of the small ribosomal subunit as well as the sarcin–ricin loop (SRL) and the 3′-CCA end of $fMet–tRNA^{Met}$ close to the peptidyl transferase centre (PTC) of the large ribosomal subunit (Fig. 1a, b). Moreover, we find ribosomal bL12m contacting the mtIF2 GTPase domain (see Extended Data Fig. 3e).

mtIF2 diverges from bacterial IF2 in several functionally important areas, despite having a conserved core fold. The mammalian mitochondrial IF2 contains an insertion of 37 amino acids between domains II and III, which forms an α-helix that extends towards the decoding centre (Fig. 1b). At the decoding centre, the helix kinks and packs against the A-site mRNA to bridge decoding nucleotides G256 (G530 in *Thermus thermophilus*) and A918/A919 (A1492/A1493 in *T. thermophilus*). This positions a Trp-Lys-X-Arg motif (corresponding to mtIF2 residues 486–489) and an aromatic side chain (residue 494)—both of which are strictly conserved—in front of the A-site codon of the mRNA (Fig. 2a, Extended Data Figs. 4, 5a, b). The mRNA extends into the P site, in which the start codon is bound by the fully accommodated $fMet–tRNA^{Met}$ (Extended Data Fig. 5c). However, there are no specific contacts between the insert and the mRNA in the A site; instead, W486 of mtIF2 stacks on top of rRNA G256, which is retained in a *syn* conformation. The mtIF2 insert then contacts helix h44, causing A919 to flip outwards and to stack with the first base of the mRNA A-site codon, which may prevent the mRNA from sliding. The decoding nucleotide A918 is not flipped outward and resides within an undistorted h44. That h44 remains undistorted during translation initiation in mitochondria contrasts with bacterial and eukaryotic initiation and re-initiation complexes[6–9]. The interactions of the mtIF2 insert with the A site resemble the interactions of bacterial IF1 with the decoding centre, although mtIF2 adopts a completely different fold[6] (Fig. 2a). This finding is consistent with an earlier genetic study showing that mtIF2 is able to substitute for *Escherichia coli* IF1 and IF2 in living cells[10], and is in line with a low-resolution structure of mtIF2 on the *E. coli* ribosome[11]. To clarify whether A-site interaction of the mtIF2 insert is required for the function of the factor, we used a recombinant *E. coli* in vitro expression system[12] (PURE system) that allows substitution of bacterial initiation factors. To ensure proper binding of the mRNA to the bacterial ribosome, the template contained a Shine–Dalgarno sequence. Therefore, the effects we observe are due to processes that occur after mRNA binding to the ribosome. We monitored in vitro translation of the model substrate DHFR–SBP (see Methods, Extended Data Fig. 8a) in reactions lacking *E. coli* IF1 and IF2 but containing mtIF2. Wild-type mtIF2 efficiently replaced bacterial initiation factors (Fig. 2c). Deletion of the Trp-Lys-X-Arg motif strongly diminishes mtIF2 function, suggesting that the mtIF2 insert increases efficiency of translation initiation—probably by excluding elongator tRNAs from premature binding to the A site and by preventing mRNA slippage to ensure correct reading frame selection. These functions are likely to be even more important for the leaderless mRNAs that are present in mitochondria, which do not form stabilizing Shine–Dalgarno interactions with mitoribosomal RNA.

Because mtIF2 does not form specific interactions with mRNA, start codon selection could occur by mitoribosome-specific mRNA engagement and subsequent threading of the mRNA into the mRNA channel for start codon–anticodon interaction. In our 28S cryo-EM map, filtered to lower resolution, *MT-CO3* mRNA is engaged with mitoribosome-specific pentatricopeptide repeat (PPR) protein mS39, which crowns the mRNA entrance (Extended Data Fig. 6a). These contacts may not be sequence- or structure-specific, as 5′ sequences of all 11 human mitochondrial mRNAs do not contain a clear consensus sequence and have been shown to exhibit no or only very weak secondary structures[13]. However, starting from codon 7, the mRNAs

[1]Department of Biology, Institute of Molecular Biology and Biophysics, ETH Zurich, Zurich, Switzerland. [2]Harry Perkins Institute of Medical Research, Centre for Medical Research, QEII Medical Centre and School of Molecular Sciences, The University of Western Australia, Nedlands, Western Australia, Australia. *e-mail: ban@mol.biol.ethz.ch

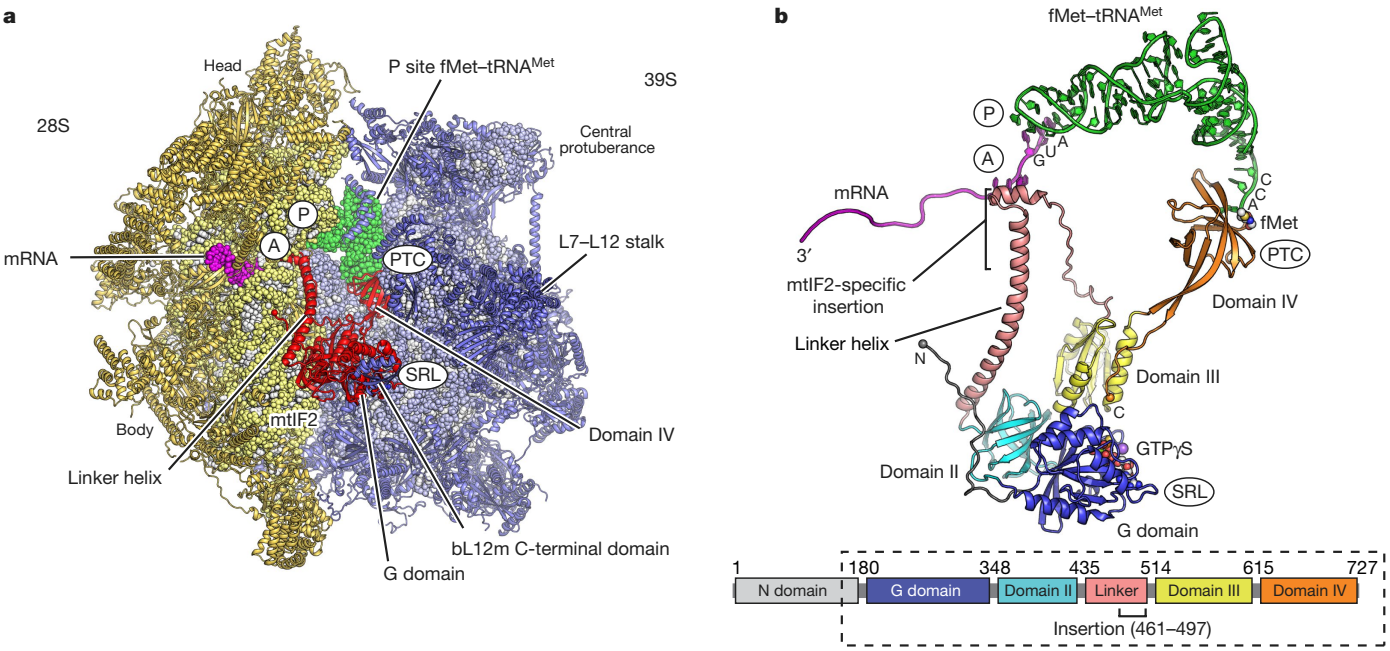

Fig. 1 | Architecture of the mammalian translation initiation complex. **a**, mtIF2 (red) bound between the small ribosomal subunit (28S, yellow) and large subunit (39S, blue) contacting initiator tRNA (green), the sarcin–ricin loop (SRL), the peptidyl transferase centre (PTC) and the decoding centre (A and P sites). **b**, Top, the ternary complex (mtIF2, fMet–tRNA^{Met} and GTPγS) displayed in isolation, with ribosomal interaction sites indicated. mtIF2 domains are colour-coded according to the schematic representation (bottom). The dashed outline indicates the part of mtIF2 visualized in our structure.

often show U as the second position nucleotide owing to encoding of hydrophobic residues in transmembrane domains (Extended Data Fig. 6d). These U-rich sequences may be the determinant for PPR association and may promote initial binding of the mitochondrial mRNAs to the initiation complex. The mRNA channel has 'tunnel'-like features and is lined with a series of positively charged conserved amino acids stemming from a mitochondrial-specific extension of uS5m (Fig. 2b, Extended Data Fig. 6b). These interactions of uS5m with the

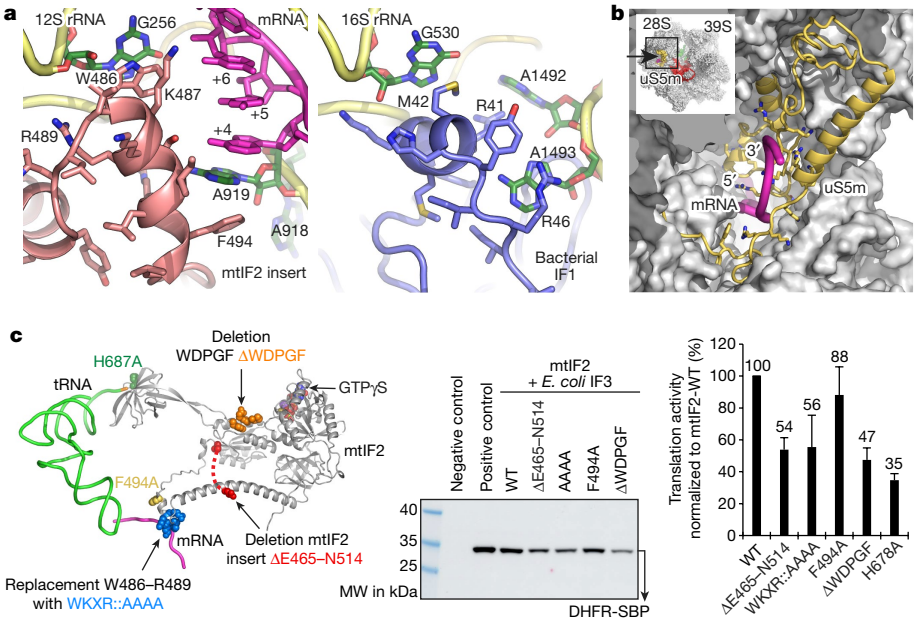

Fig. 2 | Start codon selection of leaderless mitochondrial mRNA. **a**, The mammalian-specific mtIF2 insert (salmon, left) nestles in the A site, where it interacts with decoding bases G256 and A919 in a similar fashion to bacterial IF1 (blue, right; PDB: 1HR0[6]), thereby blocking access to the bound mRNA (magenta). In the mitochondrial complex, A918 resides within helix 44, in contrast to the equivalent residue in the bacterial system, A1492, which flips outwards upon IF1 binding. **b**, The mRNA entry site is surrounded by a mammalian mitochondrial-specific extension of uS5m (yellow), which is rich in positively charged amino acids that guide the mRNA towards the A site. The small inset indicates the viewpoint. **c**, mtIF2 was substituted in place of bacterial IF1 and IF2 in an in vitro translation assay in *E. coli*. Wild-type (WT) mtIF2 and mutants were compared for efficiency of translation of the model substrate DHFR–SBP. Location and type of mtIF2 mutations are indicated. DHFR–SBP yields after 2 h at 37 °C were quantified after immunoblotting (for mtIF2(H678A), see Extended Data Fig. 8d). The negative control lacks initiation factors whereas the positive control contains *E. coli* IF1, IF2 and IF3. Data are mean ± s.d. of four independent experiments. Yields were normalized to wild-type mtIF2. For gel source data, see Extended Data Fig. 8 and Supplementary Fig. 1.

mRNA via complementary charge and the concomitant narrowing of the mRNA channel identify uS5m as an important component of the mRNA channel positioned between the entrance and the A site. uS5m appears to guide the mRNA towards the P site, where codon–anticodon interaction fixes the AUG and stabilizes the mRNA binding in frame (Extended Data Fig. 5c). Notably, in contrast to the bacterial system[14], and consistent with biochemical data[15], 5′ phosphate is not required for recruitment of leaderless mRNA as our mRNA construct loses its 5′ phosphate during hammerhead ribozyme cleavage.

In the GTPase domain of mtIF2, switch regions 1 and 2 adopt an ordered conformation and, in conjunction with the P loop, donate residues that form a hexacoordinate arrangement around a Mg^{2+} ion and two water molecules with the β- and γ-phosphates of the bound GTPγS nucleotide (Fig. 3a, Extended Data Fig. 3c). Switch 2 contains the catalytic, highly conserved H238. By analogy with cytosolic ribosomes, interaction with the phosphate backbone of the SRL should orient H238 from its inactive outwards-facing conformation to an active inward-facing conformation to induce GTP hydrolysis[16], even though our maps indicate that H238 can at least partially adopt alternative conformations on the SRL (Fig. 3a). The base of mtIF2 α-helix 12 carries a conserved Y600 residue that was hypothesized to help align the SRL with the GTPase active site of the mtIF2 orthologue in the cytosolic eukaryotic translation initiation complex[17]. The side chain of Y600 is oriented towards the catalytic H238, indicating a possible role in facilitating GTP hydrolysis (Fig. 3a). Notably, mtIF2 contains a mitochondrial-specific conserved 723-Trp-Asp-Pro-Gly-Phe-727 motif at its C-terminal tail that is absent in cytosolic orthologues and which directly contacts its switch 2 region, suggesting that the tail influences the position of the catalytic H238 (Fig. 3a, Extended Data Fig. 4). To clarify whether the C-terminal tail is required for mtIF2 function, we tested a mutant lacking the Trp-Asp-Pro-Gly-Phe motif in an in vitro translation assay as described above. Deletion of this mammalian-specific C-terminal Trp-Asp-Pro-Gly-Phe motif leads to a reduction of mtIF2 activity of approximately 50% in the *E. coli* background (Fig. 2c), indicating that it is functionally relevant, presumably by modulating the GTPase activity of the initiation factor.

Mitochondria use only one type of $tRNA^{Met}$, which is used in the form fMet–$tRNA^{Met}$ during initiation and as Met–$tRNA^{Met}$ during elongation. Thus, the sole determinant of aminoacylated $tRNA^{Met}$ that allows mtIF2 to distinguish it from elongator tRNA is the formyl group on the methionine. Formylation of Met–$tRNA^{Met}$ substantially enhances its affinity for mtIF2 and fMet–$tRNA^{Met}$ binding is independent of the nucleotide state of the factor (Fig. 3c). In the structure of the mitochondrial initiation complex, we observe the 3′-CCA end of the $tRNA^{Met}$ charged with formyl-methionine bound to domain IV of the mtIF2 (Fig. 3b). The base of A71 binds into a conserved, mostly hydrophobic pocket and the location and orientation of the methionine side chain can be unambiguously identified with hydrophobic interactions made with the side chains of F632 and A630. In this conformation, addition of the formyl group to the methionine introduces a partial negative charge that is likely to interact tightly with the surrounding D691, H678 and H679. In mtIF2, H678 is universally conserved as a side chain with the capacity to form hydrogen bonds to the formyl group, whereas in the orthologous cytosolic eIF5B, a hydrophobic residue predominates at the equivalent position, consistent with the fact that in the cytosol the methionine of initiator $tRNA^{Met}$ is not formylated and there is therefore no need for specific fMet recognition. Furthermore, in domain II of mtEF-Tu, which is involved in recognition of all amino acids except fMet and shares homology with domain IV of mtIF2, a conserved non-polar amino acid occupies an identical position (Extended Data Fig. 4). Strikingly, we observe that mutation of H678 to alanine abolishes fMet–$tRNA^{Met}$ binding to mtIF2, underlining that stable tRNA binding is critically dependent on specific hydrogen bonding interaction between fMet and mtIF2 (Figs 3c and 2c).

During initiation of translation, the exit of the ribosomal tunnel is generally thought to be vacant, owing to the absence of a nascent chain; however, in our structure, the mitochondria-specific mL45

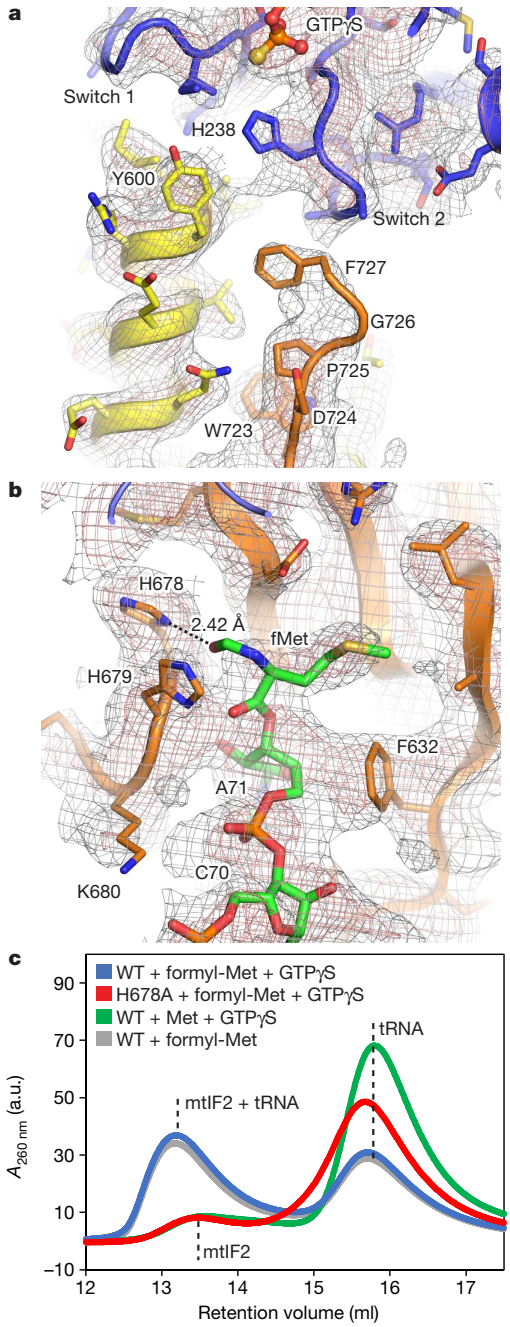

Fig. 3 | mtIF2-specific features regulate its function. a, The C terminus of mtIF2 is extended by a conserved Trp-Asp-Pro-Gly-Phe motif (orange) that reaches towards the catalytic centre of the G domain (blue). Catalytic H238 is shown in a conformation facing the γ-phosphate of GTPγS, although our maps indicate that H238 can also adopt an inactive conformation on the ribosome. mtIF2 domain III (yellow) positions the conserved Y600 close to H238 in switch 2 (map at 3 and 6σ). **b**, Interaction between the $tRNA^{Met}$-CCA-3′ end, which carries the formyl methionine (fMet), and domain IV (orange) of mtIF2. H678 stabilizes fMet binding via hydrogen bonding (dashed line). Experimental maps are shown at two contour levels (2 and 3.5σ). **c**, Size-exclusion chromatography reports on ternary complex formation. $A_{260\,nm}$ predominantly detects RNA, indicating that tRNA (23 kDa) runs separately from mtIF2 (72 kDa) if the aminoacylated tRNA is not formylated (green). fMet binding to mtIF2 shifts the tRNA peak to a higher molecular weight (blue). In solution, this interaction occurs independent of GTPγS (grey). Mutation of H678 to alanine abolishes fMet–$tRNA^{Met}$ binding to mtIF2 (red).

inserts its N-terminal tail into the polypeptide tunnel, reaching almost the entire way up to the peptidyl transferase centre (Fig. 4a). The N-terminal tail of mL45, conserved in mammals but absent in

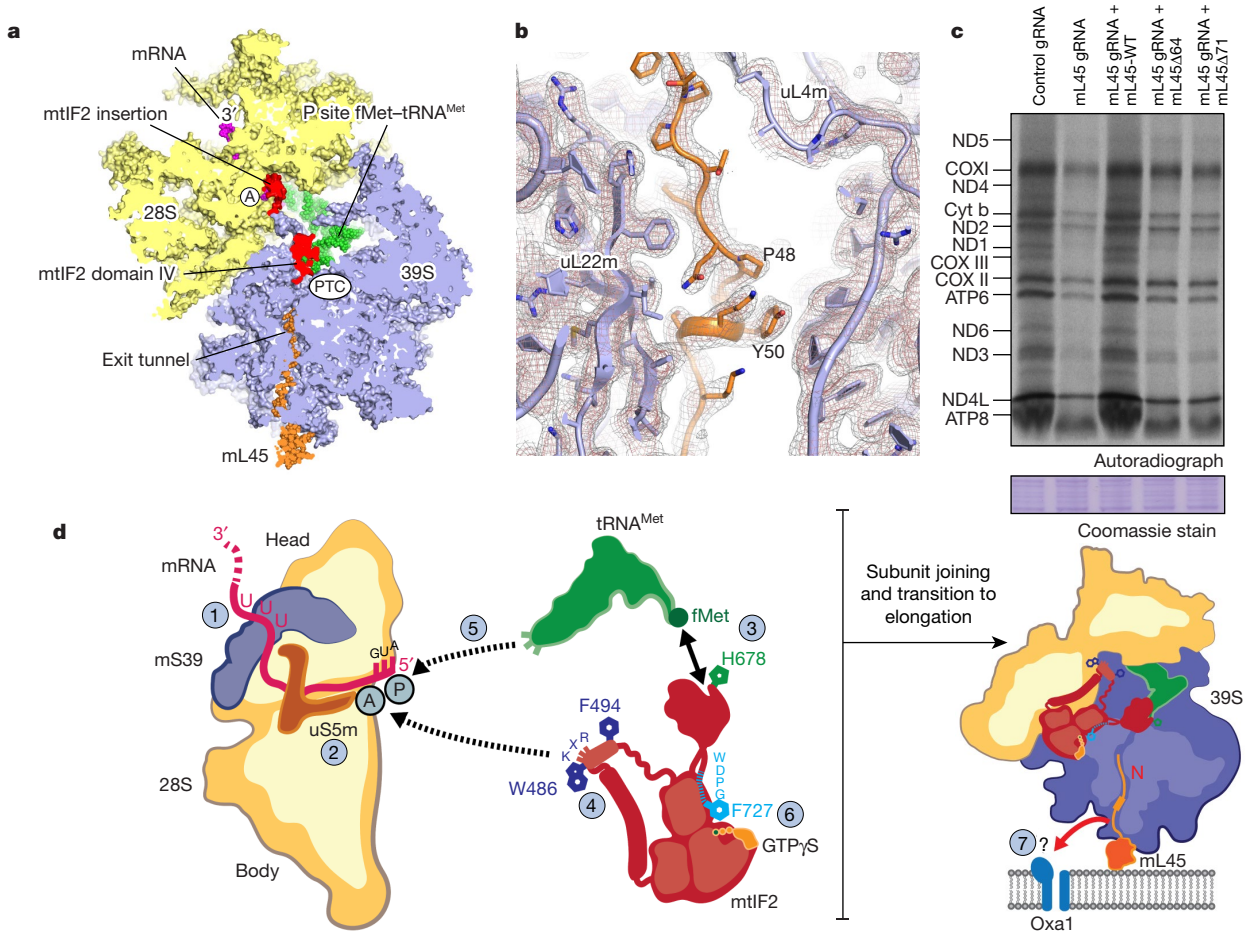

Fig. 4 | Mitochondria-specific mL45 inserts its tail into the exit tunnel. **a**, A cutaway view of the 55S translation initiation complex shows that the mL45 (orange) N-terminal extension (NTE) inserts into the vacant exit tunnel. **b**, The mL45 NTE completely blocks the exit tunnel and interacts with the constriction site. Experimental maps at 3 and 7σ. **c**, Polypeptide synthesis causes displacement of the NTE. The mL45 NTE was truncated at positions G64 and K71 to study its role in vivo. Levels of de novo protein synthesis were measured as described in Methods. Equal amounts of mitochondrial protein (determined by Coomassie staining) were separated by SDS–PAGE and visualized by autoradiography. A representative gel from three independent biological experiments is shown. **d**. Model of mammalian mitochondrial translation initiation. Numbers indicate the steps during complex assembly: 1, association of leaderless mRNA to mitochondria-specific PPR protein mS39; 2, mRNA progression towards A and P sites assisted by an extension of uS5m; 3, recognition of fMet–tRNA^{Met} by H678 of mtIF2 domain IV; 4, mtIF2 promotes fMet–tRNA^{Met} binding to the small ribosomal subunit and contacts the decoding centre with a mitochondria-specific insertion that shields the mRNA channel and may stabilize mRNA binding; 5, binding of the anticodon of fMet–tRNA^{Met} fixes the reading frame, followed by association to the large ribosomal subunit, facilitated by interactions with the bL12m CTD of the L7–L12 stalk. 39S binding induces GTP hydrolysis in mtIF2 that is; 6, likely to be additionally regulated by a C-terminal extension (F727) of the factor; 7, as the ribosome progresses from initiation to elongation, the N-terminal tail of mL45 has to be displaced and may then form a complex with the insertase Oxa1 to aid insertion and assembly of components of the respiratory chain. For gel source data, see Supplementary Fig. 1.

yeast, encompasses approximately 80 amino acids (from the predicted mitochondrial signal sequence cleavage site at L38 to N115) and is mostly devoid of secondary structure elements (Fig. 4b, Extended Data Fig. 7a, b). The extension contacts proteins uL23m and uL24m at the exit of the tunnel, inserts into the tunnel forming a small helical turn that completely fills the space between uL22m and the 16S rRNA and continues upwards, passing the narrow constriction between proteins uL22m and uL4m with two highly conserved Pro residues (Fig. 4b).

Considering that the N-terminal extension of mL45 completely blocks the tunnel, amino acids K38–N64 must be displaced from the tunnel during the elongation stage of protein synthesis (Extended Data Fig. 7c) and could then fulfill an additional function to promote membrane insertion of nascent chains. To corroborate our hypothesis, we replaced wild-type mL45 with mutants lacking the N-terminal extension in cells. CRISPR–Cas9 deletion of mL45 in HEK293T cells markedly reduced mitochondrial translation, which was recovered with the expression of a wild-type mL45, but not with mL45 lacking amino acids 45–64 or 45–71 from the N-terminal region (Fig. 4c). Levels of proteins associated with oxidative phosphorylation were also reduced upon mL45 knockout and co-expression of the truncated mL45 proteins, and the levels were rescued only by co-expression of wild-type mL45 (Extended Data Fig. 7d). These results indicate that the N terminus of mL45 is important in mitochondrial translation of membrane proteins. It is possible that the positively charged tail aids recruitment of the translocase Oxa1 to the ribosome, implicating a targeting mechanism analogous to the signal recognition particle, which is essential for the synthesis of membrane proteins in all kingdoms of life, but does not exist in mitochondria[18–20].

Online content

Any Methods, including any statements of data availability and Nature Research reporting summaries, along with any additional references and Source Data files, are available in the online version of the paper at https://doi.org/10.1038/s41586-018-0373-y

Received: 27 February 2018; Accepted: 17 May 2018;
Published online 8 August 2018.

1. Greber, B. J. et al. The complete structure of the 55S mammalian mitochondrial ribosome. *Science* **348**, 303–308 (2015).
2. Montoya, J., Ojala, D. & Attardi, G. Distinctive features of the 5′-terminal sequences of the human mitochondrial mRNAs. *Nature* **290**, 465–470 (1981).
3. Atkinson, G. C. et al. Evolutionary and genetic analyses of mitochondrial translation initiation factors identify the missing mitochondrial IF3 in *S. cerevisiae*. *Nucleic Acids Res.* **40**, 6122–6134 (2012).
4. Christian, B. E. & Spremulli, L. L. Mechanism of protein biosynthesis in mammalian mitochondria. *Biochim. Biophys. Acta* **1819**, 1035–1054 (2012).
5. Kuzmenko, A. et al. Mitochondrial translation initiation machinery: conservation and diversification. *Biochimie* **100**, 132–140 (2014).
6. Carter, A. P. et al. Crystal structure of an initiation factor bound to the 30S ribosomal subunit. *Science* **291**, 498–501 (2001).
7. Weisser, M., Voigts-Hoffmann, F., Rabl, J., Leinundgut, M. & Ban, N. The crystal structure of the eukaryotic 40S ribosomal subunit in complex with eIF1 and eIF1A. *Nat. Struct. Mol. Biol.* **20**, 1015–1017 (2013).
8. Weisser, M. et al. Structural and functional insights into human re-initiation complexes. *Mol. Cell* **67**, 447–456 (2017).
9. Lomakin, I. B. et al. Crystal structure of the human ribosome in complex with DENR–MCT-1. *Cell Reports* **20**, 521–528 (2017).
10. Gaur, R. et al. A single mammalian mitochondrial translation initiation factor functionally replaces two bacterial factors. *Mol. Cell* **29**, 180–190 (2008).
11. Yassin, A. S. et al. Insertion domain within mammalian mitochondrial translation initiation factor 2 serves the role of eubacterial initiation factor 1. *Proc. Natl Acad. Sci. USA* **108**, 3918–3923 (2011).
12. Shimizu, Y., Kanamori, T. & Ueda, T. Protein synthesis by pure translation system. *Methods* **36**, 299–304 (2005).
13. Jones, C. N., Wilkinson, K. A., Hung, K. T., Weeks, K. M. & Spremulli, L. L. Lack of secondary structure characterizes the 5′ ends of mammalian mitochondrial mRNAs. *RNA* **14**, 862–871 (2008).
14. Giliberti, J., O'Donnell, S., Etten, W. J. & Janssen, G. R. A. 5′-terminal phosphate is required for stable ternary complex formation and translation of leaderless mRNA in *Escherichia coli*. *RNA* **18**, 508–518 (2012).
15. Christian, B. E. & Spremulli, L. L. Preferential selection of the 5′-terminal start codon on leaderless mRNAs by mammalian mitochondrial ribosomes. *J. Biol. Chem.* **285**, 28379–28386 (2010).
16. Voorhees, R. M., Schmeing, T. M., Kelley, A. C. & Ramakrishnan, V. The mechanism for activation of GTP hydrolysis on the ribosome. *Science* **330**, 835–838 (2010).
17. Fernández, I. S. et al. Molecular architecture of a eukaryotic translation initiation complex. *Science* **342**, (2013).
18. Szyrach, G., Ott, M., Bonnefoy, N., Neupert, W. & Herrmann, J. M. Ribosome binding to the Oxa1 complex facilitates co-translational protein insertion in mitochondria. *EMBO* **22**, 6448–6457 (2003).
19. Keil, M. et al. Oxa1-ribosome complexes coordinate the assembly of cytochrome C oxidase in mitochondria. *J. Biol. Chem.* **287**, 34484–34493 (2012).
20. Denks, K. et al. The signal recognition particle contacts uL23 and scans substrate translation inside the ribosomal tunnel. *New Microbiol.* **2**, (2017).

Acknowledgements We thank T. Schönhut for help with purification of mtIF2 variants; A. Scaiola for support with computational problems and data analysis; V. Godinic for advice on tRNA charging; T. Schönhut, P. Bieri and M. Saurer for help with mitochondria preparation; K. Warinner for help during cloning and for creating a great working atmosphere. We would like to thank the ETH Zürich scientific centre for optical and electron microscopy (ScopeM) for access to electron microscopy equipment and P. Tittmann for technical support. E.K. was supported by an EMBO long-term fellowship (1196-2014). This work was supported by the Swiss National Science Foundation grant (310030B_163478) and via the National Centre of Excellence in RNA and Disease and project funding 138262 to N.B. We thank the NHMRC, ARC and Cancer Council of WA for grants and fellowships to A.F. and O.R. and UWA for a postgraduate scholarship to R.G.L.

Reviewer information *Nature* thanks L. Sazanov and the other anonymous reviewer(s) for their contribution to the peer review of this work.

Author contributions E.K. prepared initiation complex components, ribosomal subunits and cryo-EM samples. D.B. and E.K. acquired the cryo-EM data. E.K. calculated the cryo-EM reconstructions with support from D.B. M.L. built the atomic model and performed coordinate refinement of the atomic model. E.K., M.L. and N.B. interpreted the structure. R.G.L., O.R. and A.F. performed in vivo experiments in HEK cells. E.K. performed in vitro translation assays and size-exclusion chromatography for ternary complex formation. All authors contributed to the final version of the paper.

Competing interests : The authors declare no competing interests.

Additional information
Extended data is available for this paper at https://doi.org/10.1038/s41586-018-0373-y.
Supplementary information is available for this paper at https://doi.org/10.1038/s41586-018-0373-y.
Reprints and permissions information is available at http://www.nature.com/reprints.
Correspondence and requests for materials should be addressed to N.B.
Publisher's note: Springer Nature remains neutral with regard to jurisdictional claims in published maps and institutional affiliations.

METHODS

Plasmids. Open reading frames for MT-Co3 fused to a hammerhead ribozyme, mtIF2, mtIF3, MetRS and MTF from human mitochondria were ordered from GenScript, codon-optimized for expression in *E. coli* and subcloned into pET24a or pQE-80L vectors, respectively. mtIF2 mutants were generated by site-directed mutagenesis with the exception of mtIF2 (ΔE465–N514), in which amino acids E465–N514 are replaced by the shorter linker from *E. coli* IF2 (E675–H687). mtIF2 (ΔE465–N514) was ordered from GenScript, codon-optimized for expression in *E. coli* and subcloned into pET24a.

Plasmids co-expressing Cas9 and gRNAs were based on pD1311-AD (ATUM), which expresses nuclear localized *Streptococcus pyogenes* Cas9 fused to DasherGFP via the *Thosea asigna* virus 2A peptide. Expression cassettes for gRNAs targeting exon 1 of *mL45* (mL45 gRNA: 5′-ACAAGAGAACCCTTGAGGTA-3′) and a control gRNA targeting *EMX1* (EMX1 gRNA: 5′-TGAAGGTGTGGTTCCAGAAC-3′)[21] were synthesized from overlapping oligonucleotides and cloned into pD1311-AD. mL45 expression vectors were based on pCI-neo (Promega). The human mL45 ORF (UniProtKB - Q9BRJ2) was subcloned via NheI and NotI restriction sites and silent codon changes were introduced into the gRNA target site to preserve the encoded protein sequence while eliminating the gRNA target site. Truncation mutants of mL45 were made by deleting amino acids I45–G64 or I45–K71 (GenScript) but retaining N-terminal amino acids 1–44, which are for targeting to mitochondria and subsequent proteolytic cleavage of the mitochondrial targeting sequence.

Preparation of porcine mitochondrial subunits. Porcine mitochondria and ribosomal subunits were purified at 4 °C as described[22], with some modifications. In brief, mitochondria were dissolved in monosome buffer (20 mM HEPES-KOH pH 7.6, 100 mM KCl, 40 mM $MgCl_2$, 1 mM DTT) and lysed using a Dounce homogenizer. Triton X-100 buffer (monosome buffer including 9.6% (v/v) Triton-X100) was added to a final concentration of 1.6% (v/v) Triton X-100. The suspension was supplemented with 0.5 mM puromycin and stirred for 30 min. The lysate was cleared in two steps at 20,000 r.p.m. using a 45 Ti rotor and subsequently loaded on a 50% (w/v) sucrose cushion. After 24 h at 50,000 r.p.m. (70 Ti rotor) the supernatant was discarded and the ribosome pellet was resuspended in monosome buffer by gently shaking for 1 h on ice. 55S mitoribosomes were further purified on a 10–40% (w/v) sucrose gradient (SW 32 Ti rotor 22,500 r.p.m., 16 h) and fractions containing 55S particles were pooled. Mitoribosomes were concentrated by pelleting (SW 55 Ti rotor, 55,000 r.p.m., 5 h) and resuspended in dissociation buffer (20 mM HEPES-KOH pH 7.6, 300 mM KCl, 5 mM $MgCl_2$, 1mM DTT) by gently shaking on ice for 1 h. The suspension was cleared in two steps using a tabletop centrifuge (14,000 r.p.m., 10 min) and loaded onto a 10–40% sucrose gradient (SW 32.1 Ti, 28,000 r.p.m., 14 h). Fractions containing 39S and 28S subunits were pooled separately and subunits were concentrated by pelleting (SW 55 Ti, 55,000 r.p.m., 5h). Pellets were resuspended in 25 μl of monosome buffer containing 50 μM spermine. Rotors and centrifuges were from Beckman Coulter or Eppendorf.

Preparation of human mitochondrial initiation factors 2 and 3. Initiation factors were expressed from a pET24a vector with mtIF2 carrying an N-terminal His_6 tag followed by a TEV cleavage site and mtIF3 carrying a C-terminal His_6 tag preceded by a TEV cleavage site. Proteins were expressed in *E. coli* BL21 SI pRARE at 30 °C for 4 h and purified using a HisTrap FF 5-ml column (GE Healthcare) coupled to a HiTrap Heparin HP 5-ml column (GE Healthcare) in standard buffers (50 mM HEPES-KOH pH 7.6, 800 or 50 mM KCl, 5 mM $MgCl_2$, 10% (w/v) glycerol, 1 mM TCEP, 40 or 500 mM imidazole). The proteins were incubated with TEV protease at 4 °C overnight and the His_6 tag, uncleaved initiation factor and TEV protease were removed on a HisTrap HP 1 ml column (GE Healthcare). Proteins were subjected to size-exclusion chromatography on a HiLoad 16/60 Superdex200 (GE Healthcare) and thereby buffer exchanged into storage buffer (40 mM HEPES-KOH pH7.6, 200 mM KCl, 40 mM $MgCl_2$, 2 mM DTT, 10% (w/v) glycerol). Initiation factors were then concentrated in an Amicon Ultra-15 centrifugal filter (30-kDa MW cut-off) and flash frozen until further use.

Preparation of human mitochondrial *MT-CO3* mRNA. The *MT-CO3* gene, encoded as a hammerhead–CO3 construct[23] in a pUC19 vector and under control of a T7 promoter, was digested with StyI to generate a template that was suitable for T7 run-off transcription. The restriction site was chosen such that transcription would yield an mRNA of approximately 200 nucleotides in length[24]. The template was purified by phenol-chloroform extraction and subsequent ethanol precipitation. In vitro transcription (40 mM Tris-HCl pH 7.2, 30 mM $MgCl_2$, 0.01% (v/v) Triton X-100, 5 mM DTT, 1 mM spermidine, 10 mM NTPs) was performed at 37 °C for 5 h and transcripts were incubated for 1 h at 60 °C to complete hammerhead cleavage. mRNA was separated from the hammerhead ribozyme using preparative urea PAGE (5% polyacrylamide, 1× TBE, 6 M urea). The appropriate band was excised from the gel, ground into pieces and mRNA was extracted over night at 4 °C by shaking the gel pieces in water. The mRNA was then buffer exchanged in an Amicon Ultra-15 (10-kDa MW cut-off) to remove residual urea and concentrate the mRNA before flash freezing it until further use.

Purification of human MetRS and MTF. Human mitochondrial methionyl-tRNA synthetase (MetRS) was purified without the first 42 amino acids, as they contain the mitochondrial import sequence. The protein was expressed from a pQE-80L vector in *E. coli* BL21 carrying the pG-KJE8 chaperone plasmid (TAKARA Bio) at 18 °C over night. First, MetRS was affinity purified using an N-terminal His_6 tag (HisTrap FF 5ml, GE Healthcare) in 50 mM HEPES-KOH pH 7, 300 mM KCl, 20% (w/v) glycerol, 1 mM TCEP and 40 or 500 mM imidazole. The eluted sample from the affinity column was diluted in low salt buffer and applied to a HiTrap Heparin HP 5 ml column (GE Healthcare) using HEPES-KOH pH 7.0, 50 or 500 mM KCl, 20% (w/v) glycerol and 1 mM TCEP. MetRS fractions were pooled and concentrated in an Amicon Ultra-15 (30-kDa MW cut-off) before flash freezing.

Methionyl-tRNA formyl transferase (MTF) was expressed from a pQE-80L vector in *E. coli* BL21 for 5 h at 30 °C. The protein carries an N-terminal His_6 tag and was affinity purified on a HisTrap FF 5-ml column (GE Healthcare) in buffers as described for mitochondrial initiation factors and subsequently buffer exchanged into storage buffer (20 mM HEPES-KOH pH7.6, 100 mM KCl, 10% (w/v) glycerol, 1 mM DTT). MTF was flash frozen and stored until further use.

Purification, charging and formylation of human mitochondrial $tRNA^{Met}$. Mitochondrial $tRNA^{Met}$ was produced from a construct described as a hammerhead fusion[23]. In brief, BstNI digestion was used to generate a template that would result in a CCA-3′ end on the transcription product. In vitro transcription, hammerhead cleavage and tRNA purification were carried out as described for the MT-CO3 mRNA. The $tRNA^{Met}$ was stored in water. To induce folding of the $tRNA^{Met}$, it was diluted to 0.5 mg/ml in water, heated to 80 °C for 5 min, supplemented with $MgCl_2$ to a final concentration of 10 mM and kept at room temperature for 20 min before storing on ice. Leucovorin (Schircks Laboratories) was converted into 10-formyltetrahydrofolate (10-CHO-THF) as described[25], to be used as the formyl donor. Aminoacylation and formylation were performed in aminoacylation buffer (50 mM HEPES-KOH pH 7.6, 100 mM NaCl, 10 mM $MgCl_2$, 5 mM β-mercaptoethanol). Folded $tRNA^{Met}$ was mixed with 2 mM L-methionine, 5 mM ATP, 400 μM MetRS and incubated for 40 min at 30 °C before adding 300 μM 10-CHO-THF and 1 μM MTF) and keeping the reaction for another 15 min at 30 °C. fMet–$tRNA^{Met}$ was purified by phenol-chloroform extraction and subsequent ethanol precipitation. fMet–$tRNA^{Met}$ pellets were dissolved in monosome buffer. Aliquots were flash frozen and stored at −80 °C until further use.

Preparation of translation initiation complex. The initiation complex was assembled starting from ribosomal subunits in analogy to canonical eukaryotic or bacterial translation initiation. First, the ternary complex was formed by incubating 10 μM mtIF2, 10 μM fMet–$tRNA^{Met}$ and 4 mM GTPγS for 4 min at 37 °C. Then, 60 nM 28S subunits were mixed with 250 nM *MT-CO3* mRNA and 250 nM mtIF3. mtIF3 was included to increase efficiency of initiation complex formation[26]. After 2 min at 37 °C, the ternary complex was added in a 1:20 dilution (that is, final concentrations are 500 nM mtIF2, 500 nM fMet–$tRNA^{Met}$ and 200 μM GTPγS). In the 55S initiation complex, the 39S subunit (final concentration 60 nM) was added after 3 more min at 37 °C and was allowed to associate the small subunit at 37 °C for 3 min before placing the initiation complex on ice for 15 min until grid preparation was started. The sample was applied to Quantifoil R2/2 holey carbon grids (Quantifoil Micro Tools) coated with a thin continuous carbon film. The grids were flash frozen in pure ethane on a Vitrobot (FEI).

Data collection and image processing. Images were collected in movie mode on a FEI Titan Krios cryo-electron microscope equipped with a Falcon III direct electron detector (FEI) at 300 kV with a total dose of 40 e/Å^2 subdivided into 28 frames in 1.4-s exposure using EPU version 1.9.0.30REL (FEI). Images were recorded at 100,719× magnification and a defocus range from −1.2 to −2.4 μm. Movie frames were aligned, summed and weighted by dose in MOTIONCOR2[27,28] using 5×5 patches, and CTF estimation and particle selection was done using GCTF[29] and BATCHBOXER[30]. Micrographs that contained large pieces of ice or showed poor particle distribution or carbon wrinkles were removed after visual inspection. After CTF estimation we rigorously excluded micrographs that did not reach a resolution higher than 3.2 Å. Particles were picked and initial 3D classification was performed using the 55S mitoribosome (excluding tRNAs in A and P sites) as a reference[1].

We collected three datasets that were first processed separately. Particle images (4× binned) were subjected to initial 2D and 3D classification in RELION2[31] to isolate the population of reassembled 55S ribosomes before further local 3D classifications was used focusing on mtIF2, the small ribosomal subunit and the A site, as shown in the included classification schemes (Extended Data Fig. 1). Masks applied for focused 3D classification in the early steps of particle sorting focused either on mtIF2 G domain, domain II and domain III (mask I) to remove particles that had no mtIF2 bound, or on the connection between mtIF2 domain IV and fMet–$tRNA^{Met}$ (mask III) to remove particles that did not contain tRNA. After initial sorting, our three datasets were joined. We found that

in different classification approaches different parts of the initiation complex were resolved best during further particle sorting and decided to work with 3 different maps that were refined to high resolution in RELION2 and used for model building (Extended Data Figs. 1, 2).

Map 1 and map 2 were generated aligning full size particle images on the small ribosomal subunit in 3D refinement (gold-standard) using a mask surrounding the entire small subunit (mask IV). Subsequently, during focused 3D classification (mask IV) without further alignment particles were removed that still contained no or only poorly associated small ribosomal subunit and the remaining particles were aligned on the small subunit in another round of 3D refinement (mask IV). The mtIF2 insert that resides in the A site is rather flexible, which necessitated one more round of local 3D classification using a mask surrounding the A site that included the small mtIF2 α-helical element deposited in the A site, part of the mRNA and the codon–anticodon pair (mask III). Three-dimensional classification yielded a particle set that showed clear density for codon-anticodon interaction and the mtIF2 insert in front of the mRNA codon located in the A site. These particles were refined either over the entire particle volume (yielding map 1) or using a mask surrounding the small ribosomal subunit (mask IV, yielding map 2). Despite extensive particle sorting, the mediocre local resolution (Extended Data Fig. 2) of the large ribosomal subunit in map 2 also illustrates that the ribosomal subunits show a substantial degree of rotational freedom in the mitochondrial initiation complex. Map 2 was used for general revision of the small ribosomal subunit as well as model building of the mtIF2 insert and the mitochondria-specific extension of uS5m.

Map 3 was generated by another round of focused 3D classification of 4×-binned particle images with the mask surrounding mtIF2 G domain, domain II and domain III (mask I). Three-dimensional classification resulted in two major classes that differed in the degree of subunit rotation and resolution for mtIF2. The class with excellent density for mtIF2 was refined to high resolution over the entire particle volume using unbinned particle images and showed high local resolution used especially for interpretation of the large ribosomal subunit, mL45 and mtIF2.

Structure building and refinement. The structures of the small 28S and the large 39S ribosomal subunit were built into the cryo-EM maps that had been calculated using focused classification (maps 2 and 3 in Extended Figs. 1a, 2). For this, structures of the porcine subunits (PDB: 4V19, 4V1A and 5AJ3)[1,32] were docked as rigid bodies, followed by fitting of individual proteins and rRNA segments. The increased resolution and high quality of the maps allowed a general structural update, which included building of more complete rRNA and protein models, adjustments of protein side chains and nucleotide conformers using manual model rebuilding in O[33] and COOT[34] (Extended Data Table 1). For the previously not decorated PPR folds at the 28S head (mS39) and body (mS27) and rRNA h44, the homologous human mitoribosomal structure served as an additional guide (PDB: 3J9M)[35]. Although resolved to lower local resolution, secondary structure elements of the L7–L12 stalk proteins and the C-terminal domain of bL12 were readily visible, allowing unambiguous docking of Phyre2[36] homology models into these regions (PDB: 1ZAV[37] for the L7–L12 stalk and 1CTF[38] for the bL12-CTD, respectively) (Supplementary Table 1).

Remaining density representing human mtIF2 was initially interpreted by docking IF2 domains of homologous bacterial high-resolution X-ray structures (PDB: 1G7T[39], 4KJZ[40]) and an NMR structure of mouse mtIF2 domain IV (PDB: 2CRV). The model was then manually rebuilt and completed, which included extending the linker helix towards the A site and building of the mitochondrial-specific insertion between domain II and III into the cryo-EM map of the small subunit (map 2), where this segment of mtIF2 was better resolved. Owing to lower local resolution, the linker that connects the insertion from the A site back to domain III (residues 496–513) was modelled as UNK (Supplementary Table 1). For the tRNA, a high-resolution structure of $tRNA^{Phe}$ (PDB: 1EHZ[41]) served as starting model. The acceptor arm of the human mitochondrial fMet–$tRNA^{Met}$ was then rebuilt into map 3 encompassing the large subunit, where the CCA-3′ end with the attached formyl-methionine moiety was resolved at atomic resolution. The tRNA was completed by building the anticodon stem into the small subunit map 2 (Supplementary Table 1).

Phase-restrained coordinate refinement in PHENIX.REFINE[42] was performed in reciprocal space against the MLHL target using amplitudes and phases back-calculated from the experimental cryo-EM maps as described[32]. For this, the cryo-EM maps were masked around the individual subunits together with the tRNA and mtIF2, which were present in both models. Each subunit was then individually refined for 7 cycles including rigid body, individual coordinate and B-factor refinement (Supplementary Table 2). Automatic protein secondary structure and RNA base-pair restraints as well as Ramachandran restraints were applied throughout to stabilize the refinement in areas of weaker density. The weighting of the model geometry versus the experimental data (implemented in PHENIX.REFINE as wxc value) was adjusted such that the models displayed excellent geometry with an optimal fit to the cryo-EM map (Supplementary Table 2). The model was validated by calculating the model versus map FSCs using the FSC = 0.5 criterion, showing that the estimated resolutions coincide well with those obtained for the experimental maps at the FSC = 0.143 criterion (Extended Data Fig. 2b).

For the 55S initiation complex, both subunit models were assembled into the map encompassing the entire ribosome. The complete 55S model was then refined in reciprocal space for an additional 3 cycles with refinement settings as described above, followed by 5 cycles of individual B-factor refinement until convergence. The model was validated against the 55S map in a similar manner as depicted for the individual subunits.

Size-exclusion chromatography of the ternary complex. mtIF2 (15 μM), 4 μM mitochondrial $tRNA^{Met}$ (aminoacylated or aminocylated and formylated, respectively) and 2 mM GTPγS were incubated in monosome buffer for 10 min at 37 °C and 5 min on ice before separation on a Superdex 200 10/300 GL column (GE Healthcare). Mitochondrial $tRNA^{Met}$ was traced at 260 nm. The presence of isolated $tRNA^{Met}$ in the tRNA peak and as fMet–$tRNA^{Met}$ in complex with mtIF2 in the complex peak was verified by urea or SDS–PAGE, respectively (data not shown).

In vitro translation assays. PURE Express kits were purchased from New England Biolabs with *E. coli* IF1, IF2 and IF3 delivered in separate vials. mtIF2 variants were generated by site-directed mutagenesis and purified as described above. mRNA encoding human DHFR coupled to streptactin binding protein (SBP) and containing an ribosomal binding site (RBS, Extended Data Fig. 8a) was prepared using run-off transcription as described above. Assays were carried out in reaction volumes of 10 μl according to manufacturer's instructions with DHFR-mRNA as template at a final concentration of 2 μM. A negative control lacking all *E. coli* initiation factors as well as a positive control containing *E. coli* IF1, IF2, IF3 was included, showing that our generated mRNA was efficiently translated only if all *E. coli* initiation factors were present. The activity of mtIF2 variants in the PURE Express system was characterized in the presence of *E. coli* IF3. First, reactions were incubated at 37 °C for 2 h, keeping the IF3 concentration constant and adding mtIF2(WT) at concentrations ranging from 0.05 μM to 4 μM to deduce the concentration at which mtIF2 was present in saturating amounts (Extended Data Fig. 8b). We chose to continue our experiments with mtIF2 at 0.3 μM concentration, since this reflected the middle of the linear activity range, meaning that if mtIF2 variants show stronger or weaker activity than wild type we should be able to detect these differences. Five microlitres of each reaction was applied to 12% SDS PAGE and subsequently immunoblotted using anti-SBP-HRP antibodies (Santa Cruz, SB19-C4). Immunoblots were stained using the ECL Western Blotting Detection Reagent (Amersham) and recorded on an Amersham Imager 600. Immunoblots were quantified using the gel analysis routine in ImageJ (http://rsb.info.nih.gov/ij/index.html) and normalized to the activity of mtIF2(WT).

Cell culture and transfections. Human embryonic kidney (HEK293T) cells were cultured at 37 °C in humidified 95% air/5% CO_2 in Dulbecco's modified essential medium (DMEM) (Gibco, Life Technologies) containing glucose (4.5 g/l), L-glutamine (2 mM), 1mM sodium pyruvate and 50 μg/ml uridine, fetal bovine serum (FBS) (10%, v/v), penicillin (100 U/ml), and streptomycin sulfate (100 μg/ml). HEK293T cells were plated at 60% confluence in six-well plates and transfected with mammalian expression plasmids in OptiMEM medium (Invitrogen). One hundred and fifty-eight nanograms per centimetre squared of mL45 plasmid DNA and mL45 CRISPR/Cas9 plasmid DNA were transfected using Fugene HD (Roche). Cell incubations were carried out for up to 72 h following transfection and the cells were sorted for fluorescence using a FACSAria II (BD Biosciences). Sorted cells were allowed to recover until they reached 80% confluence and de novo protein synthesis was measured as described below.

The cells were obtained from ATCC, authenticated by STR profiling and found to be free of mycoplasma.

Translation assay. De novo protein synthesis was analysed as previously described[43]. In brief, HEK293T cells were grown in six-well plates until 80% confluent and de novo protein synthesis was analysed. The growth medium was replaced with methionine and cysteine-free medium containing 10% dialysed FBS for 30 min before addition of 100 μg/ml emetine for 5 min. Next, 200 μCi Express35S Protein Labelling Mix [35S] (Perkin–Elmer) was added and incubated at 37 °C for 1 h, then cells were washed in PBS and collected by trypsinization. The cells were suspended in PBS, 20 μg of proteins were separated on 12.5% SDS PAGE and the radiolabelled proteins were visualized on film.

Steady-state levels of oxidative phosphorylation complexes. Specific proteins were detected using a rabbit monoclonal antibodies against mL45 (16394-1-AP) and bS16m (16735-1-AP), and mouse monoclonal antibodies: Total OXPHOS Cocktail Antibody (ab110412) and β-actin (ab8226). All primary antibodies were diluted 1:1000 using Odyssey blocking buffer (LI-COR). IR Dye 800CW Goat Anti-Rabbit IgG or IR Dye 680LT Goat Anti-Mouse IgG (LI-COR) secondary antibodies (diluted 1:10000) were used and the immunoblots were visualized using the Odyssey Infrared Imaging System (LI-COR).

Sucrose gradients of mitochondrial ribosomes to analyse mL45 mutant incorporation. Sucrose gradient fractionation was carried out on mitochondria isolated from cells, as previously described[44].

Figure generation. Molecular graphics were generated using PyMOL (Schroedinger) or the UCSF Chimera package[45].

Reporting summary. Further information on experimental design is available in the Nature Research Reporting Summary linked to this paper.

Data availability. The coordinates and corresponding cryo-EM maps were deposited in the Protein Data Bank (PDB) and in the Electron Microscopy Data Bank (EMDB) under accession codes 6GAZ and EMD-4369 (28S small ribosomal subunit), 6GB2 and EMD-4370 (39S large ribosomal subunit), and 6GAW and EMD-4368 (55S initiation complex). All other data can be obtained from the corresponding authors upon reasonable request.

21. Ran, F. A. et al. Double nicking by RNA-guided CRISPR Cas9 for enhanced genome editing specificity. *Cell* **154**, 1380–1389 (2013).
22. Greber, B. J. et al. Architecture of the large subunit of the mammalian mitochondrial ribosome. *Nature* **505**, 515–519 (2014).
23. Spencer, A. C., Heck, A., Takeuchi, N., Watanabe, K. & Spremulli, L. L. Characterization of the human mitochondrial methionyl-tRNA synthetase. *Biochemistry* **43**, 9743–9754 (2004).
24. Liao, H. X. & Spremulli, L. L. Effects of length and mRNA secondary structure on the interaction of bovine mitochondrial ribosomes with messenger RNA. *J. Biol. Chem*. **265**, 11761–11765 (1990).
25. Blanquet, S., Dessen, P. & Kahn, D. Properties and specificity of methionyl-$tRNA_f^{Met}$ formyltransferase from *Escherichia coli*. *Methods Enzymol*. **106**, 141–152 (1984).
26. Koc, E. C. & Spremulli, L. L. Identification of mammalian mitochondrial translation initiation factor 3 and examination of its role in initiation complex formation with natural mRNAs. *J. Biol. Chem*. **277**, 35541–35549 (2002).
27. Grant, T. & Grigorieff, N. Measuring the optimal exposure for single particle cryo-EM using a 2.6 Å reconstruction of rotavirus VP6. *eLife* **4**, (2015).
28. Zheng, S. Q. et al. MotionCor2: anisotropic correction of beam-induced motion for improved cryo-electron microscopy. *Nat. Methods* **14**, 331–332 (2017).
29. Zhang, K. Gctf: real-time CTF determination and correction. *J. Struct. Biol*. **193**, 1–12 (2016).
30. Ludtke, S. J., Baldwin, P. R. & Chiu, W. EMAN: semiautomated software for high-resolution single particle reconstructions. *J. Struct. Biol*. **128**, 82–97 (1999).
31. Scheres, S. H. RELION: implementation of a Bayesian approach to cryo-EM structure determination. *J. Struct. Biol*. **180**, 519–530 (2012).
32. Greber, B. J. et al. The complete structure of the large subunit of the mammalian mitochondrial ribosome. *Nature* **515**, 283–286 (2014).
33. Jones, T. A. Interactive electron-density map interpretation: from INTER to O. *Acta Crystallogr. D* **60**, 2115–2125 (2004).
34. Emsley, P., Lohkamp, B., Scott, W. G. & Cowtan, K. Features and development of Coot. *Acta Crystallogr. D* **66**, 486–501 (2010).
35. Amunts, A., Brown, A., Toots, J., Scheres, S. H. W. & Ramakrishnan, V. The structure of the human mitochondrial ribosome. *Science* **348**, 95–98 (2015).
36. Kelley, L. A., Mezulis, S., Yates, C. M., Wass, M. N. & Sternberg, M. J. The Phyre2 web portal for protein modeling, prediction and analysis. *Nat. Protocols* **10**, 845–858 (2015).
37. Diaconu, M. et al. Structural basis for the function of the ribosomal L7/12 stalk in factor binding and GTPase activation. *Cell* **121**, 991–1004 (2005).
38. Leijonmarck, M. & Liljas, A. Structure of the C-terminal domain of ribosomal protein L7/L12 from *Escherichia coli* at 1.7 Å. *J. Mol. Biol*. **195**, 555–579 (1987).
39. Roll-Mecak, A., Cao, C., Dever, T. E. & Burley, S. K. X-ray structures of the universal translation initiation factor IF2/eIF5B: conformational changes on GDP and GTP binding. *Cell* **103**, 781–792 (2000).
40. Eiler, D., Lin, J., Simonetti, A., Klaholz, B. P. & Steitz, T. A. Initiation factor 2 crystal structure reveals a different domain organization from eukaryotic initiation factor 5B and mechanism among translational GTPases. *Proc. Natl Acad. Sci. USA* **110**, 15662–15667 (2013).
41. Shi, H. & Moore, P. B. The crystal structure of yeast phenylalanine tRNA at 1.93 Å resolution: a classic structure revisited. *RNA* **6**, 1091–1105 (2000).
42. Adams, P. D. et al. PHENIX: a comprehensive Python-based system for macromolecular structure solution. *Acta Crystallogr. D* **66**, 213–221 (2010).
43. Rackham, O. et al. Pentatricopeptide repeat domain protein 1 lowers the levels of mitochondrial leucine tRNAs in cells. *Nucleic Acids Res*. **37**, 5859–5867 (2009).
44. Rackham, O. et al. Hierarchical RNA processing is required for mitochondrial ribosome assembly. *Cell Reports* **16**, 1874–1890 (2016).
45. Pettersen, E. F. et al. UCSF Chimera—a visualization system for exploratory research and analysis. *J. Comput. Chem*. **25**, 1605–1612 (2004).
46. Chen, V. B. et al. MolProbity: all-atom structure validation for macromolecular crystallography. *Acta Crystallogr. D* **66**, 12–21 (2010).
47. Fernandez-Leiro, R. & Scheres, S. H. W. A pipeline approach to single-particle processing in RELION. *Acta Crystallogr. D*. **73**, 496–502 (2017).
48. Wahl, M. C. & Möller, W. Structure and function of the acidic ribosomal stalk proteins. *Curr. Protein Pept. Sci*. **3**, 93–106 (2002).
49. Helgstrand, M. et al. The ribosomal stalk binds to translation factors IF2, EF-Tu, EF-G and RF3 via a conserved region of the L12 C-terminal domain. *J. Mol. Biol*. **365**, 468–479 (2007).
50. Tourigny, D. S., Fernández, I. S., Kelley, A. C. & Ramakrishnan, V. Elongation factor G bound to the ribosome in an intermediate state of translocation. *Science* **340**, (2013).
51. Pallesen, J. et al. Cryo-EM visualization of the ribosome in termination complex with apo-RF3 and RF1. *eLife* **2**, (2013).
52. Kuhle, B. & Ficner, R. A monovalent cation acts as a structural and catalytic cofactor in translational GTPases. *EMBO J*. **33**, 2547–2563 (2014).
53. Selmer, M. et al. Structure of the 70S ribosome complexed with mRNA and tRNA. *Science* **313**, 1935–1942 (2006).
54. Dolinsky, T. J., Nielsen, J. E., McCammon, J. A. & Baker, N. A. PDB2PQR: an automated pipeline for the setup of Poisson-Boltzmann electrostatics calculations. *Nucleic Acid Res*. **32**, W665–W667.
55. Baker, N. A., Sept, D., Joseph, S., Holst, M. J. & McCammon, J. A. Electrostatics of nanosystems: application to microtubules and the ribosome. *Proc. Natl Acad. Sci. USA* **98**, 10037–10041 (2001).
56. Li, L. et al. DelPhi: a comprehensive suite for DelPhi software and associated resources. *BMC Biophys*. **4**, (2012).
57. Englmeier, R., Pfeffer, S. & Förster, F. Structure of the human mitochondrial ribosome studied *in situ* by cryoelectron tomography. *Structure* **25**, 1574–1581 (2017).

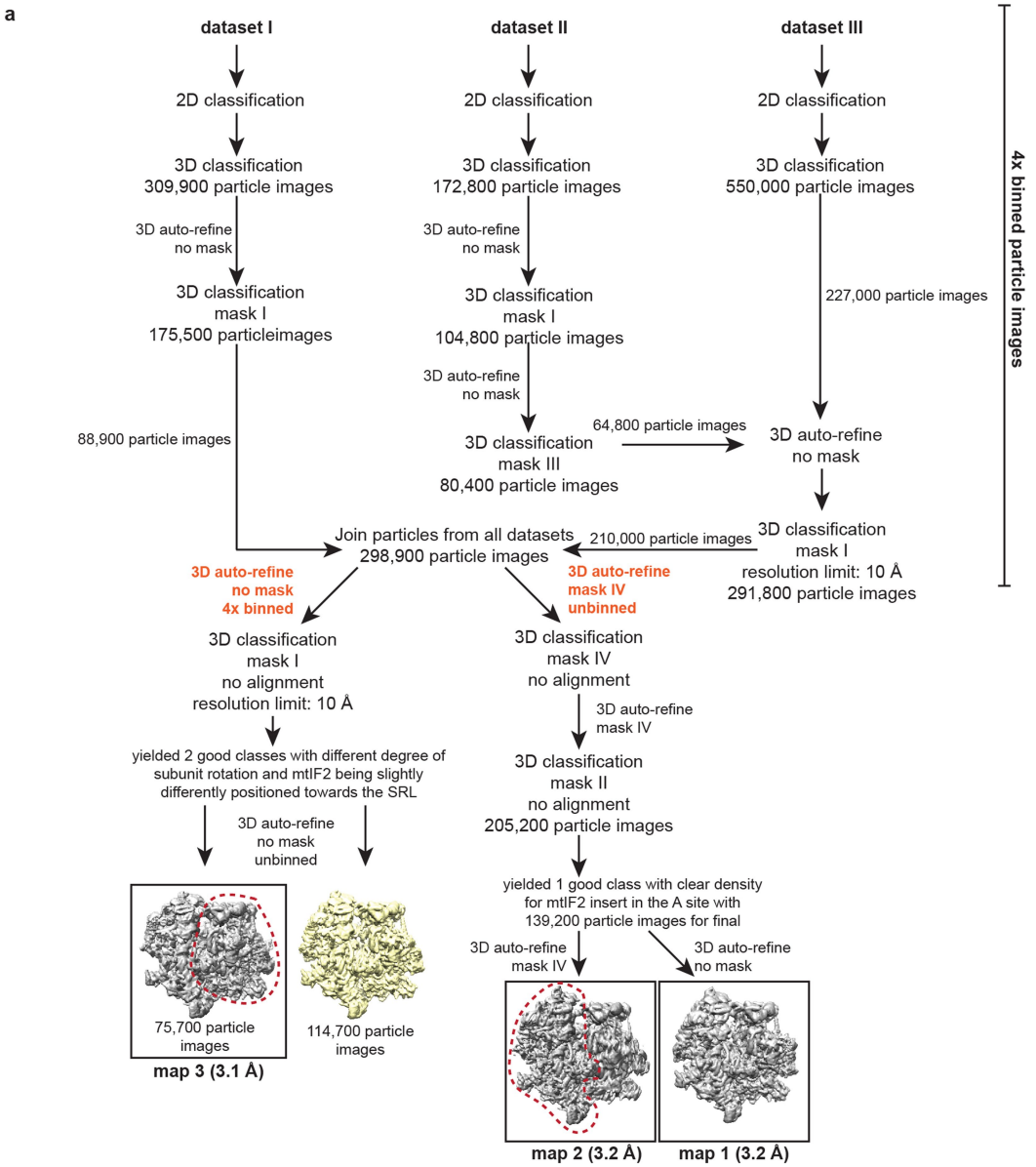

Extended Data Fig. 1 | Classification scheme. a, Schematic representation of how the different cryo-EM maps have been calculated in RELION[31,47]. Classification yielded three maps used for model building. Maps 1 and 2 were calculated from identical particles with map 1 being refined over the entire particle volume whereas map 2 refinement was focused on the 28S subunit of the ribosome. Map 3 derived from a different particle subset and was refined over the entire particle volume. Resolutions have been estimated in RELION by post-processing the entire ribosome (map 1), 28S including mtIF2 and tRNA (map 2, indicated in red) or 39S including mtIF2 and tRNA (map 3, indicated in red). **b**, Depiction of masks that have been applied for focused 3D classification or 3D refinement in RELION. Mask I encompasses the mtIF2 G domain, domain II and domain III. Mask II includes the 28S A site and the mtIF2 insert. Mask III focuses on fMet–tRNA^{Met} and domain IV of mtIF2. Mask IV includes the 28S subunit.

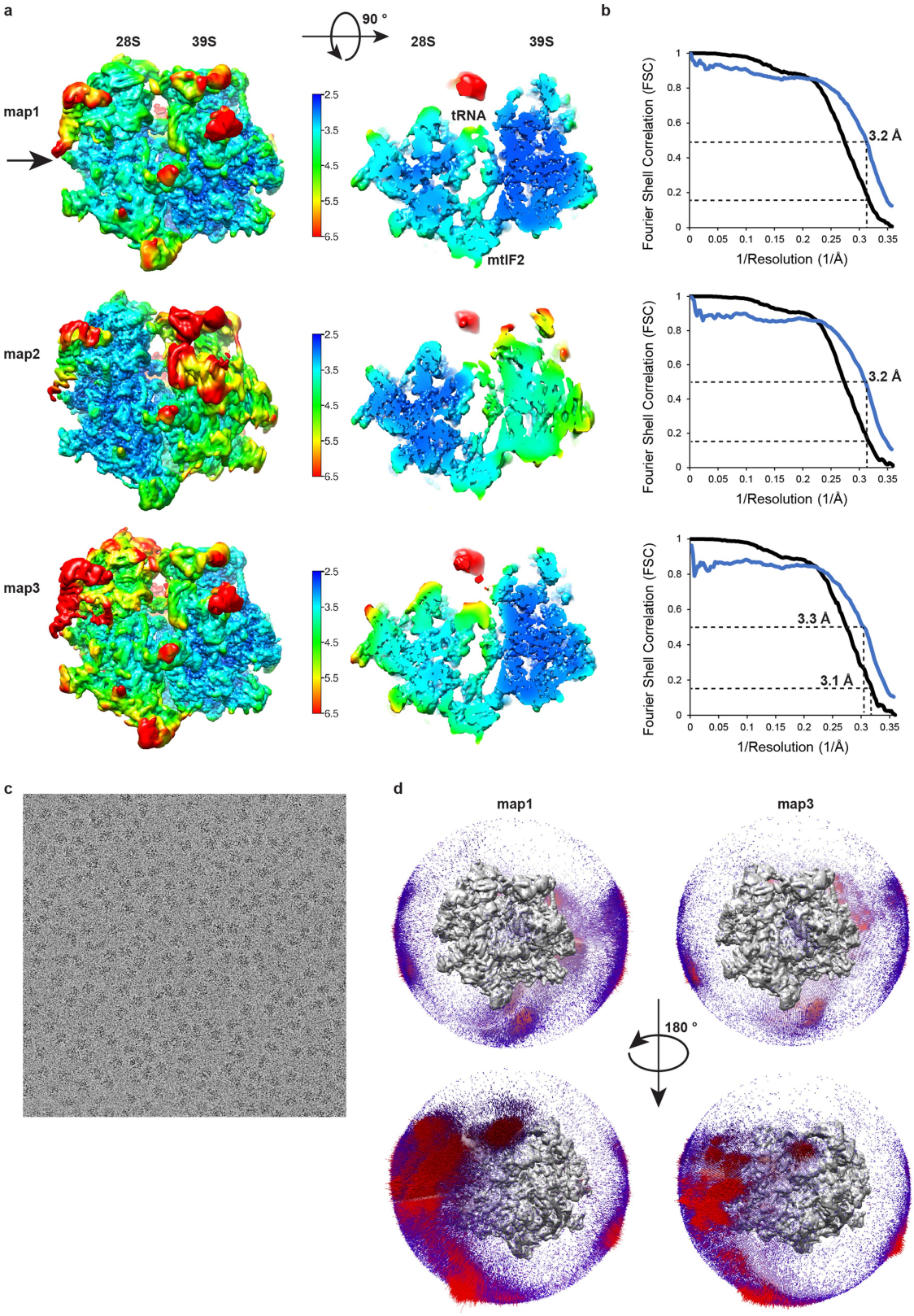

Extended Data Fig. 2 | See next page for caption.

Extended Data Fig. 2 | Map evaluation. a, Local resolution estimation performed in RELION yielded maps that were filtered according to the local resolution estimate[47]. Displayed are a front view and a slabbed view at a position indicated by the arrow on the left. Colour keys indicate the local resolution in Å. In contrast to the FSC curves in Extended Data Fig. 2b, local resolution has been estimated and depicted for the entire volume of map 1, map 2 and map 3. Map 2 indicates that the ribosomal subunits exhibit a substantial rotational freedom in the initiation complex leading to a poorly resolved 39S if the alignment is focused on the 28S during refinement. **b**, FSC curves calculated from the two particle half sets from gold-standard 3D refinement (black) or from model versus map (blue) for all three deposited maps and their corresponding PDBs. **c**, A representative micrograph shows the particle distribution of the 55S initiation complex on cryo-EM grids. **d**, Euler angle distribution of particles included in the final 3D reconstructions are shown using the .bild file generated in Relion. Distributions for map 1 and map 3 are displayed. Because map 1 and map 2 were generated from the same particle subset, map 2 distribution is expected to be very similar to the one from map 1 and is therefore not shown.

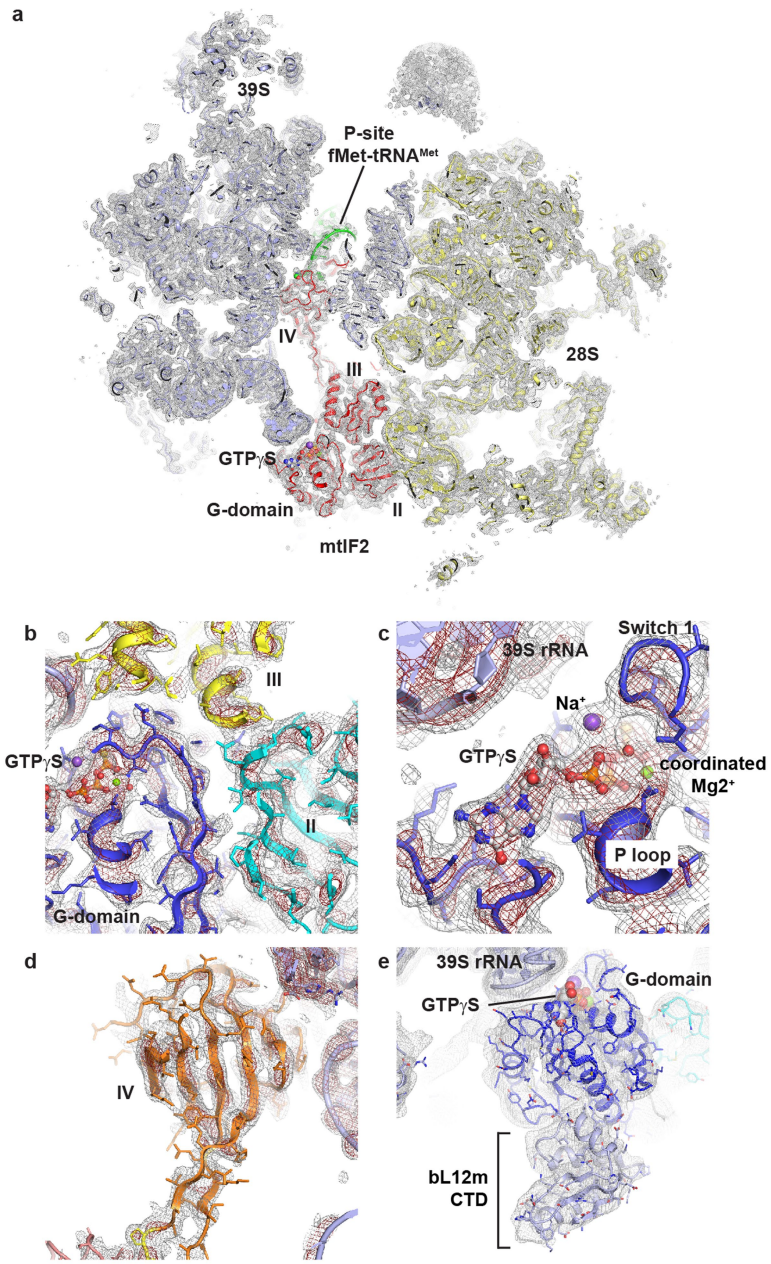

Extended Data Fig. 3 | Quality of the cryo-EM maps around mtIF2 and the role of C-terminal domain of bL12m in subunit joining. a, Sliced representation of the ternary complex (red) bound between the ribosomal subunits. All domains of mtIF2 are clearly resolved (maps at 2.2 and 4σ). **b**–**e**, Magnified views of different areas of mtIF2. **b**, The contact site of the G domain with domains II and III (maps at 3 and 6σ). **c**, GTPγS coordinated by the mtIF2 P loop and switch regions 1 and 2 (maps at 2.75 and 5.5σ). **d**, Domain IV (maps at 2.75 and 5.5σ). **e**, Map filtered to 5 Å showing bL12m-CTD bound to the solvent-side of the mtIF2 G-domain and opposite to GTPγS. The ribosomal L7–L12 stalk forms part of the conserved GTPase activating centre of the ribosomal large subunit in all kingdoms of life[48]. It enhances recruitment of translational GTPases to cytoplasmic ribosomes via its flexibly attached C-terminal domain (CTD), which has been observed to bind the G′ domains in EF-G and RF3[49–51]. However, G′ does not exist in mtIF2. In the initiation complex, we show that bL12m-CTD recognizes the G-domain of mtIF2 on the surface-exposed side opposite the catalytic centre. Since initiation complex formation involves binding of mtIF2 to the small ribosomal subunit before the large subunit joins, the observed interactions of mtIF2 with bL12m may be important to promote subunit joining to form the 55S mitoribosomal initiation complex rather than recruitment of mtIF2 to the assembled ribosome. The bL12m-CTD was modelled with PHYRE2[36] using PDB 1CTF[38] as a template and docked as a rigid body. Experimental densities are shown at two different contour levels (1.5 and 3σ).

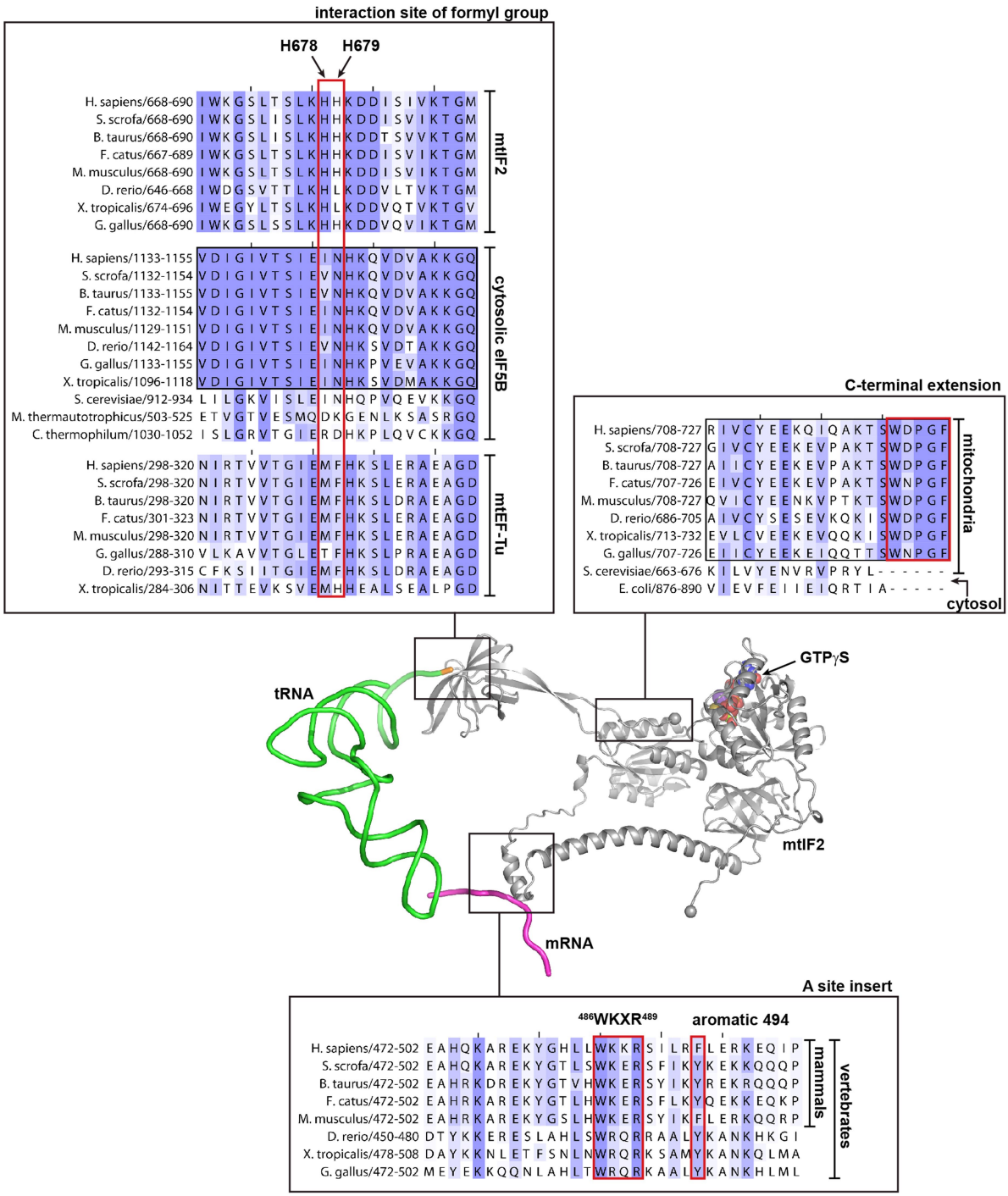

Extended Data Fig. 4 | Sequence alignments for different functionally important regions of mtIF2. Boxes indicate where the aligned sequences are located. The alignments contain sequences from mammals as well as other vertebrates to depict a more general conservation. The alignment for the fMet interaction site also contains eIF5B homologues for which structures have already been published (*Saccharomyces cerevisiae*[17], *Methanothermobacter thermautotrophicus*[39], *Chaetomium thermophilum*[52]). The alignment for the C-terminal extension of mtIF2 also contains *S. cerevisiae* mtIF2 and cytosolic IF2 from *E. coli*, both of which lack the extension.

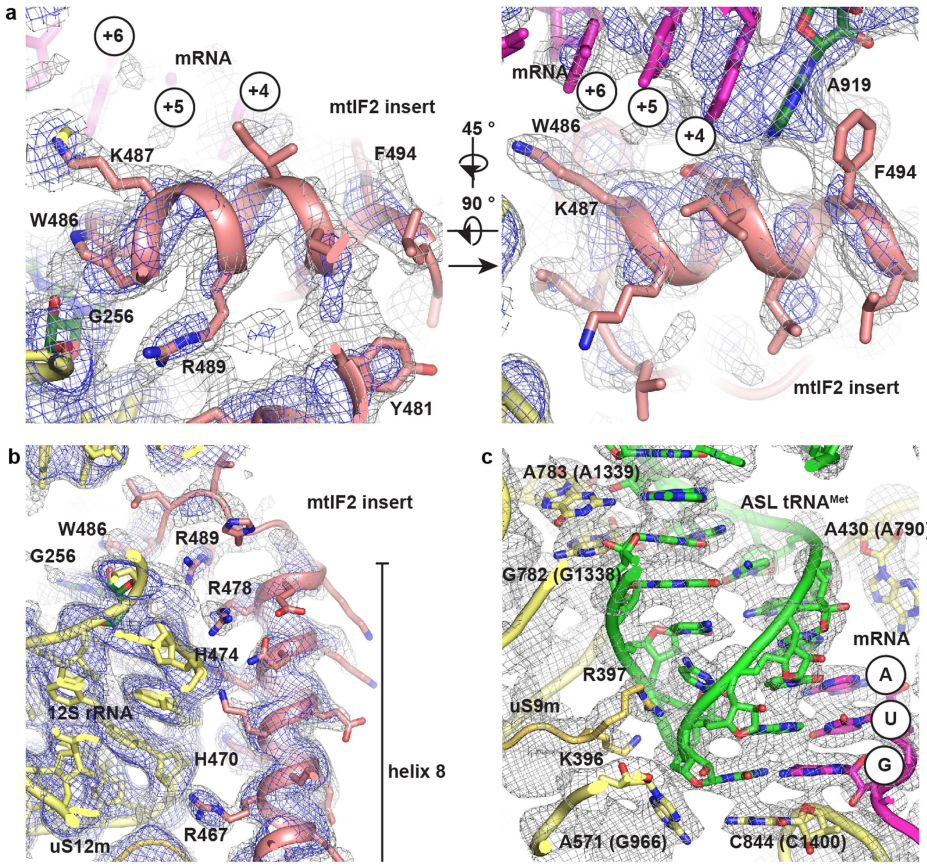

Extended Data Fig. 5 | The mtIF2 insert contacts the decoding centre and closes the mRNA channel. a, Two views of the α-helical element of the mtIF2 insert occupying the A site with experimental maps at two different contour levels (maps at 3 and 5σ). W486 stacks on top of decoding nucleotide G256 and F494 contacts the flipped out A919. mRNA bases are numbered according to their position relative to the 5′ end of the mRNA. **b**, The mtIF2 insert substantially extends α-helix 8 of the mitochondrial IF2 homologue and then enters the A site. A stable contact is established by a number of conserved positively charged residues facing the 12S rRNA (maps at 3 and 5σ). **c**, The fMet–tRNA^{Met} anticodon stem loop (ASL) that is in contact with the *MT-CO3* AUG start codon is stabilized in the P site by numerous conserved interactions with 12S rRNA[53]. The anticodon fully base-pairs with the start codon, with the tRNA wobble base of the anticodon stacking on top of C844 (C1400 in *T. thermophilus*) and its ribose against A571 (G966). G782/A783 (G1338/A1339) protrude from the 28S head to form A-minor interactions with fMet–tRNA^{Met} specific G–C pairs 26:38 and 27:37. A430 (A790) stacks onto the ribose of tRNA nucleotide 35 to stabilize tRNA binding from the opposite side of the ASL. Protein uS13 is not present in mitoribosomes und thus uS9m is the only ribosomal protein to contact tRNA in the P site. Its C-terminal tail (comprising residues K396 and R397) reaches into a cavity formed by phosphates 30, 31 and 31 of the ASL backbone (map at 5σ).

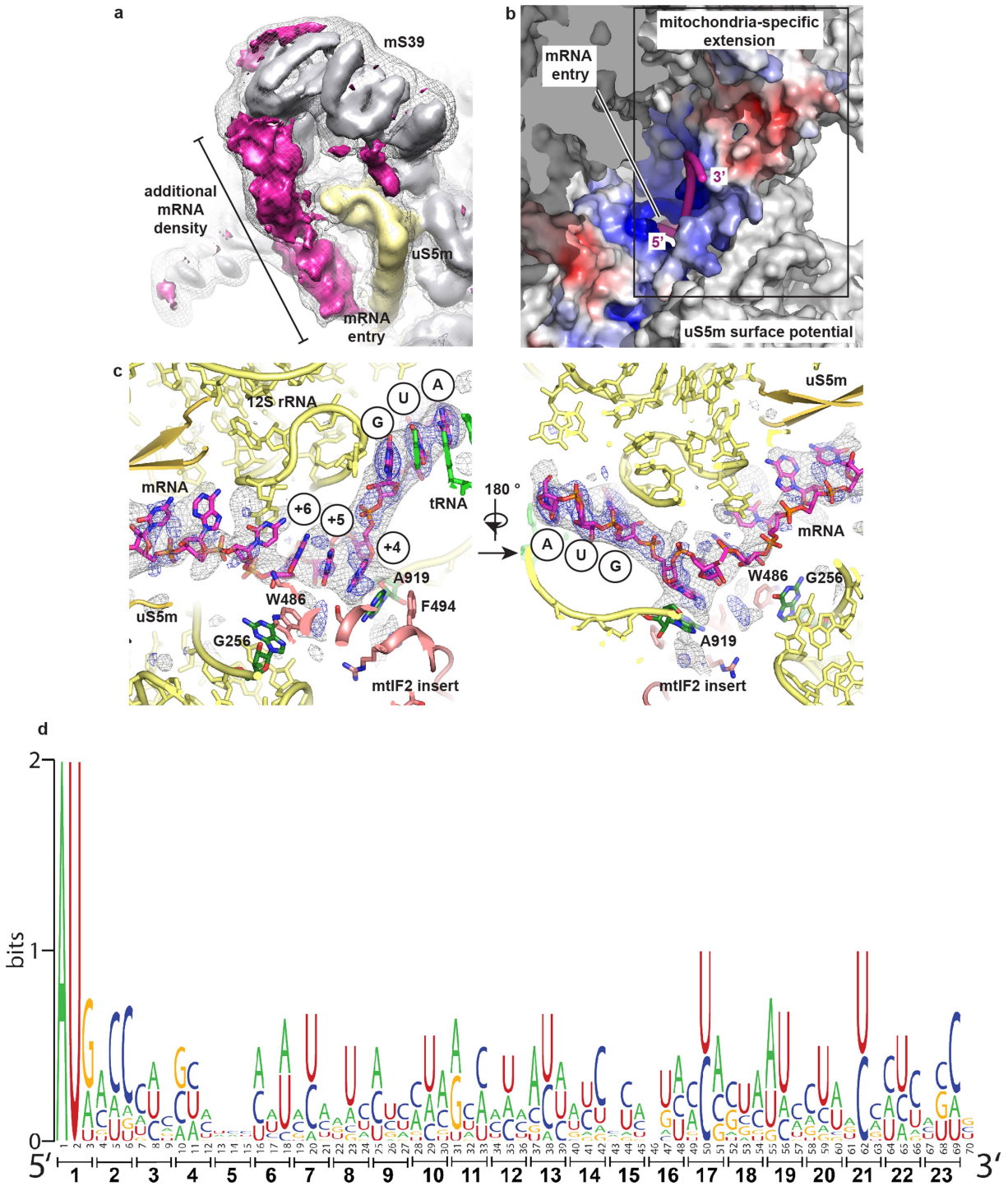

Extended Data Fig. 6 | See next page for caption.

Extended Data Fig. 6 | mRNA binding and start codon selection on the mitochondrial ribosome. a, Map 2 (classified for as described in Extended Data Fig. 1 and displayed without post-processing) shown colour coded according to the underlying atomic coordinates (grey, the small ribosomal subunit and mtIF2; yellow, uS5m). A lower contour level of map 2 is shown in transparency and locally filtered in Relion[47]. Density that cannot be assigned to the underlying atomic coordinates reaches from mS39 towards the mRNA entry site (magenta). We believe that this density contains mostly mRNA but it may also include 6 unassigned amino acids from mS39 and possibly part of 21 unassigned amino acids from the N terminus of mS35. **b**, The mRNA entry is surrounded by uS5m. mRNA (magenta) follows the positively charged surface of the mitochondria-specific uS5m extension towards the A site. The surface potential for uS5m was calculated using PDB 2PQR[54] and visualized with the APBS tool[55] from PyMOL (M. Lerner and H. Carlson, University of Michigan). ± 5 kT/e electrostatic potential of uS5m have been plotted. **c**, Although resolved to atomic resolution only in the area of the start codon–anticodon interaction, cryo-EM density for the mRNA can be assigned along its entire path through the mRNA channel, reaching from the P site—where the AUG start codon is located—into the A site, which is shielded by the mtIF2 insert. Subsequently, density nestles alongside protein uS5m, which substantially restricts the diameter of the mRNA channel and places a delineation that may prevent mRNA from slipping out of the mRNA channel. Map 2 is shown unfiltered (blue) and filtered to 5 Å (grey) at two contour levels. For clarity, cryo-EM density for the entire ribosome and mtIF2 has been subtracted from map 2 in Chimera and the difference density is carved 10 Å around our modelled mRNA (contour levels are 10 and 15σ). The mRNA occupies a similar position as in the elongation complex[1]. **d**, Alignment of the first 70 nucleotides of the 11 mRNA 5′ ends in human mitochondria (*MT-ND1*, *MT-ND2*, *MT-CO1*, *MT-CO2*, *MT-ATP8*, *MT-CO3*, *MT-ND3*, *MT-ND4L*, *MT-ND5*, *MT-CYB*, *MT-ND6*), starting precisely at the start codon. Codons are indicated by bars and numbered. Alignments were generated using the weblogo server (https://weblogo.berkeley.edu).

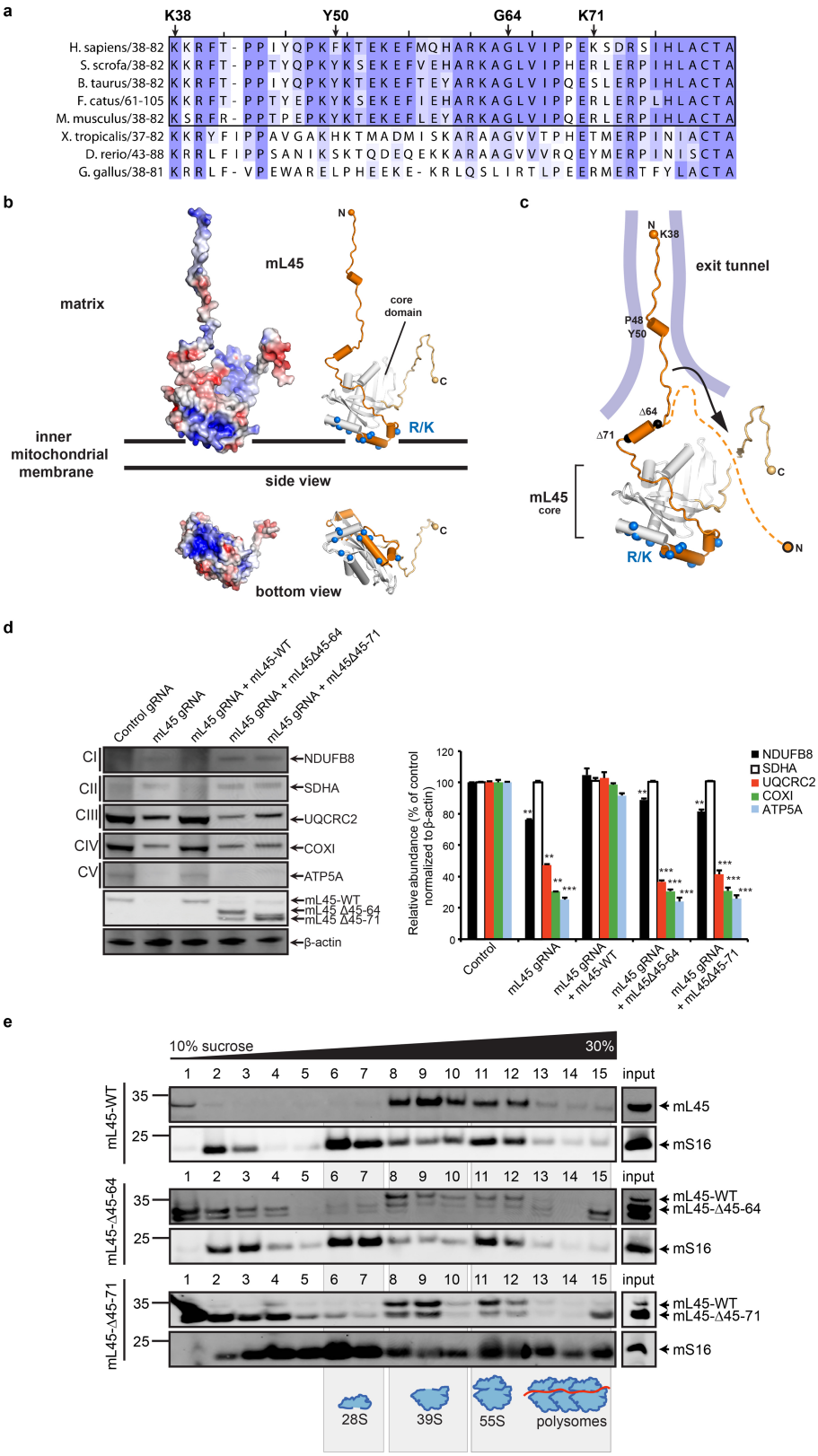

Extended Data Fig. 7 | See next page for caption.

Extended Data Fig. 7 | mL45 serves as ribosomal membrane anchor and is crucial for insertion of oxidative phosphorylation proteins. **a**, Sequence alignment of the mL45 N-terminal extension in vertebrates shows strong sites of conservation—predominantly in mammals. **b**, The surface potential of mL45 (calculated using DELPHI implemented in MOLDRAW[56] and visualized with the APBS tool of PyMOL) shows that the membrane-facing side of mL45 contains a large positively charged patch that may mediate association to the negatively charged inner mitochondrial membrane[57]. For comparison, the structure is shown as a cartoon in the right panel, with positions of positively charged residues in the putative membrane interaction area as blue spheres. **c**, Polypeptide synthesis necessitates displacement of the NTE at a hinge region around G64. The mL45 NTE was truncated at positions G64 and K71 to study its role in vivo. Locations of positively charged residues in mL45 α-helices proposed to mediate membrane association of the ribosome are indicated as blue spheres. **d**, Left, cell lysates (25 μg) from HEK293T cells co-transfected with control or mL45 CRISPR/Cas9 plasmids and MRPL45 wild type or deletion mutant expressing plasmids were resolved on 4–20% SDS–PAGE gels and immunoblotted to investigate the steady-state levels of nuclear- and mitochondrial-encoded oxidative phosphorylation (OXPHOS) and ribosomal proteins. β-actin was used as a loading control. The data are representative of at least three independent biological experiments. Right, quantification of the relative abundance of the OXPHOS polypeptides relative to control and normalized to the β-actin loading control. Error bars indicate standard error of the mean. $^{**}P < 0.01$, $^{***}P < 0.001$, Student's *t*-test. **e**, A continuous 10–30% sucrose gradient was used to determine the distribution of the small and large ribosomal subunit and polysomes in mitochondria isolated from cells expressing wild-type or truncated mL45. Mitochondrial ribosomal protein markers of the small (bS16m) and large (mL45) ribosomal subunits were detected by immunoblotting. The input, mitochondrial lysate, was used as a positive control. For gel source data, see Supplementary Fig. 1.

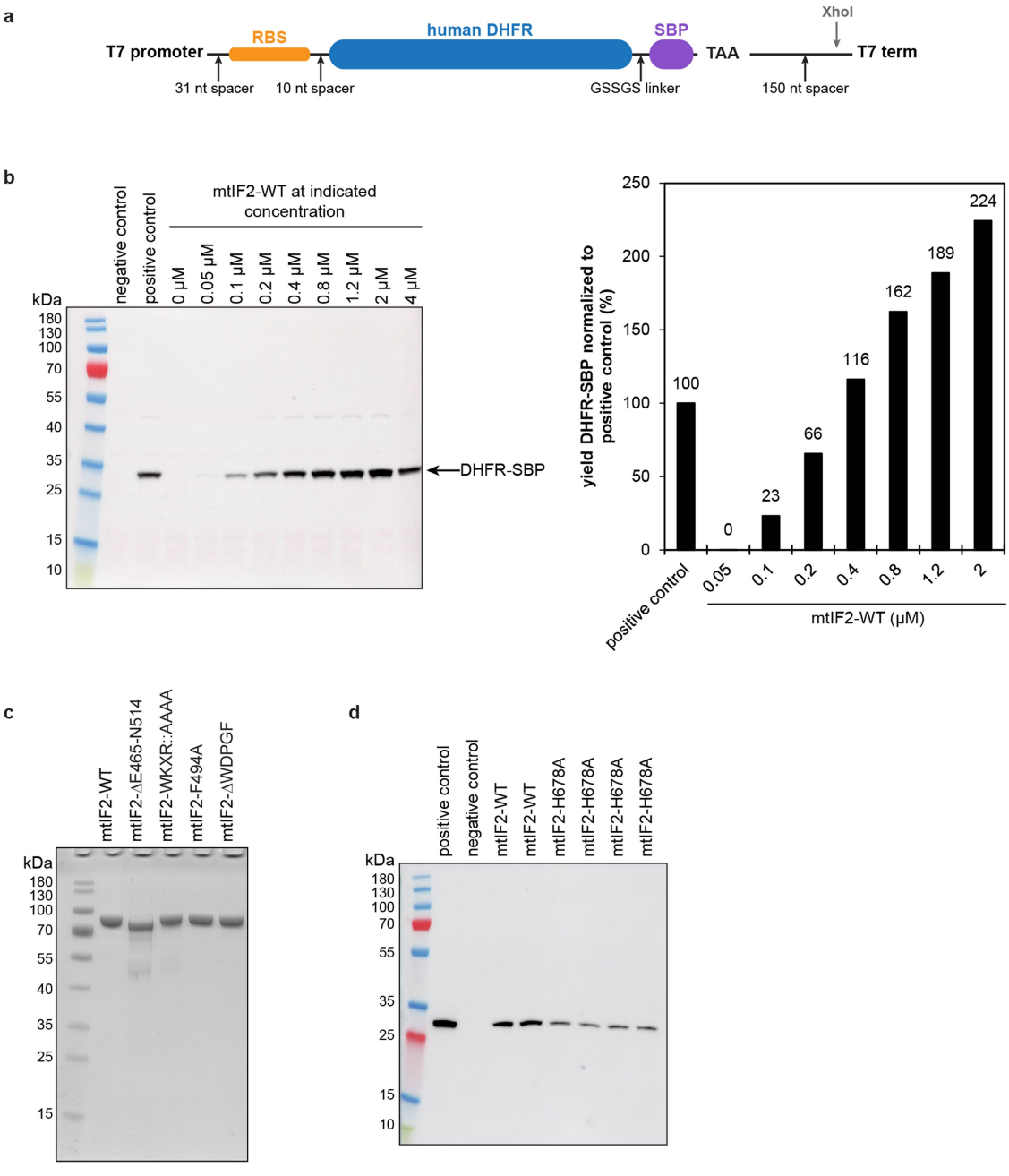

Extended Data Fig. 8 | Additional information on in vitro translation assays. a, Depiction of the construct used for in vitro translation assays. Human DHFR was fused to streptactin binding protein (SBP) via a linker encoding the amino acid sequence GSSGS. Ribosome binding site (RBS), linker regions (nt, nucleotides) as well as T7 promoter and terminator have been copied from the PURE Express template plasmid provided by the manufacturer (New England Biolabs). The XhoI cleavage site was used to generate DNA templates for run-off transcription. DHFR–SPB was efficiently expressed either upon addition of DNA as template or after supplying DHFR–SBP mRNA directly (data not shown). We decided to perform all subsequent experiments providing equal amounts of mRNA to ensure that every sample contains the same concentration of template in order to make translation yields comparable. **b**, Production of DHFR–SBP was monitored after 2 h at 37 °C at different concentrations of mtIF2(WT). The positive control contained *E. coli* IF1, IF2 and IF3 but no mtIF2. The negative control contained all *E. coli* initiation factors but lacked mRNA. mtIF2 was tested at the given concentrations and in the presence of *E. coli* IF3. Immunoblots (left) were quantified using the gel analysis routine in ImageJ (right). The sample containing 4 µM mtIF2 was excluded from quantification because it was only partially transferred onto the nitrocellulose membrane during blotting. **c**, SDS–PAGE with 2 µg protein loaded for each mtIF2 variant to show that protein concentrations have been estimated correctly for all variants before in vitro translation was performed (data for mtIF2(H678A) not shown). **d**, Since experiments to determine the translation activity of mtIF2(H678A) were performed at a later time point than for other variants, samples were analysed on separate immunoblots. The immunoblot shows samples from 4 independent experiments for mtIF2(H678A) and 2 independent experiments for mtIF2(WT). Bands have been quantified as for other mtIF2 variants using the gel analysis routine in ImageJ and activity was normalized to mtIF2(WT) (see Fig. 2).

Extended Data Table 1 | Cryo-EM data collection and refinement statistics

EM Data collection			
Microscope model	FEI Titan Krios		
Detector model	FEI Falcon 3EC		
Number of datasets	3		
Number of micrographs collected	13936		
Magnification	100719x		
Voltage (kV)	300		
Electron dose (e^{-}Å^{-2})	40		
Pixel size (Å)	1.39		
Defocus range (μm)	1.2 – 2.5		
Symmetry imposed	none		
Name of 3D-reconstruction	28S subunit[a]	39S subunit[b]	55S initiation complex
EMDB map entry	EMD-4369	EMD-4370	EMD-4368
PDB coordinate entry	PDB 6GAZ	PDB 6GB2	PDB 6GAW
Initial particle images (no.)	1,366,787	1,366,787	1,366,787
Final particles images (no.)	139,206	75,666	139,206
Resolution (Å) (at FSC = 0.143)	3.2	3.1	3.2
Map sharpening B-factor (Å^2)	-151.5	-140.5	-83.2
Reciprocal space refinement and model validation statistics[c]			
Initial model used (PDB code)	4v1a	4v19	6GAZ/6GB2
Model resolution (Å) (at FSC = 0.5)	3.2	3.3	3.2
Map resolution range used for refinement (Å)	40.0-3.13	40.0-3.13	40.0-3.15
Map sharpening B-factor (Å^2)	-151.5	-140.5	-83.2
Spacegroup	P1	P1	P1
a=b=c (Å)	390.59	390.59	390.59
α=β=γ (°)	90	90	90
Number of reflections	4057133	4056927	3972521
Model composition			
Non-hydrogen atoms	73170	111114	178376
Protein residues	6303	9311	15043
RNA residues	1048	1687	2664
Ligands[d]	125	228	347
B factors			
Average	73.8	56.9	66.8
Protein	83.3	64.4	75.4
RNA	52.3	41.6	48.7
Ligands[d]	59.8	30.6	37.6
Working R-factor (%)	24.7	24.4	28.0
wxc weighting factor	1.25	1.25	1.25
R.m.s. deviations			
Bond lengths (Å)	0.008	0.006	0.007
Bond angles (°)	1.098	1.017	0.949
Validation[c]			
MolProbity score	2.56	2.54	2.53
Clashscore	11.4	9.4	10.2
Protein			
Poor rotamers (%)	9.6	10.1	9.2
EMRinger score	2.228102	2.339295	1.940439
Ramachandran plot (%)			
Favored	96.4	95.9	96.0
Allowed	3.5	4.0	3.9
Disallowed	0.1	0.1	0.1
RNA			
Correct sugar puckers (%)	99.6	99.4	99.5

[a]During refinement of the 28S small subunit, mtIF2, the mRNA and fMet–tRNA^{Met} were included.
[b]During refinement of the 39S large subunit, mtIF2 and fMet–tRNA^{Met} were included.
[c]The model was validated using the MolProbity server (http://molprobity.biochem.duke.edu)[46].
[d]Ligands include Mg, Na, Zn, HOH, spermine, GTPγS, GTP, GMP and formyl-methionine.

nature research

Corresponding author(s): Nenad Ban

Reporting Summary

Nature Research wishes to improve the reproducibility of the work that we publish. This form provides structure for consistency and transparency in reporting. For further information on Nature Research policies, see Authors & Referees and the Editorial Policy Checklist.

Statistical parameters

When statistical analyses are reported, confirm that the following items are present in the relevant location (e.g. figure legend, table legend, main text, or Methods section).

n/a	Confirmed	
☐	☒	The exact sample size (*n*) for each experimental group/condition, given as a discrete number and unit of measurement
☐	☒	An indication of whether measurements were taken from distinct samples or whether the same sample was measured repeatedly
☐	☒	The statistical test(s) used AND whether they are one- or two-sided *Only common tests should be described solely by name; describe more complex techniques in the Methods section.*
☒	☐	A description of all covariates tested
☐	☒	A description of any assumptions or corrections, such as tests of normality and adjustment for multiple comparisons
☐	☒	A full description of the statistics including central tendency (e.g. means) or other basic estimates (e.g. regression coefficient) AND variation (e.g. standard deviation) or associated estimates of uncertainty (e.g. confidence intervals)
☐	☒	For null hypothesis testing, the test statistic (e.g. *F*, *t*, *r*) with confidence intervals, effect sizes, degrees of freedom and *P* value noted *Give P values as exact values whenever suitable.*
☒	☐	For Bayesian analysis, information on the choice of priors and Markov chain Monte Carlo settings
☒	☐	For hierarchical and complex designs, identification of the appropriate level for tests and full reporting of outcomes
☒	☐	Estimates of effect sizes (e.g. Cohen's *d*, Pearson's *r*), indicating how they were calculated
☐	☒	Clearly defined error bars *State explicitly what error bars represent (e.g. SD, SE, CI)*

Our web collection on statistics for biologists may be useful.

Software and code

Policy information about availability of computer code

Data collection	Images were collected in movie mode on a FEI Titan Krios cryo-electron microscope equipped with a Falcon III direct electron detector (FEI company) at 300 kV with a total dose of 40 e/Å2 subdivided into 28 frames in 1.4 s exposure using EPU version 1.9.0.30REL (FEI company). Images were recorded at 100719 x magnification and a defocus range from -1.2 to -2.4 µm.
Data analysis	Movie frames were aligned, summed and weighted by dose in MOTIONCOR2 using 5x5 patches, and CTF estimation and particle selection was done using GCTF and BATCHBOXER. Calculations of 2D class averages, 3D class averages, 3D refinement according to gold-standard and B factor sharpening has been done in Relion2 as well as local resolution estimation. Manual model building was done in O and COOT. Phase-restrained coordinate refinement was perfomed in PHENIX.REFINE.

For manuscripts utilizing custom algorithms or software that are central to the research but not yet described in published literature, software must be made available to editors/reviewers upon request. We strongly encourage code deposition in a community repository (e.g. GitHub). See the Nature Research guidelines for submitting code & software for further information.

Data

Policy information about availability of data

All manuscripts must include a data availability statement. This statement should provide the following information, where applicable:

- Accession codes, unique identifiers, or web links for publicly available datasets
- A list of figures that have associated raw data
- A description of any restrictions on data availability

The coordinates and corresponding EM maps were deposited in the Protein Data Bank (PDB) and in the Electron Microscopy Data Bank (EMDB) under accession codes PDB 6GAZ and EMD-4369 (28S small ribosomal subunit), PDB 6GB2 and EMD-4370 (39S large ribosomal subunit), and PDB 6GAW and EMD-4368 (55S initiation complex). All other data can be obtained from the corresponding authors upon reasonable request.

Field-specific reporting

Please select the best fit for your research. If you are not sure, read the appropriate sections before making your selection.

☒ Life sciences ☐ Behavioural & social sciences ☐ Ecological, evolutionary & environmental sciences

For a reference copy of the document with all sections, see nature.com/authors/policies/ReportingSummary-flat.pdf

Life sciences study design

All studies must disclose on these points even when the disclosure is negative.

Sample size	Biochemistry: At least 3 replicates have to be included to allow statistical analysis.
Data exclusions	No data exclusion.
Replication	3 cryo-EM datasets were collected yielding a total number of 1366787 particle images for further classification. In vivo and in vitro biochemical experiments were perfomed at least in 3 independent replicats and assessed statistically.
Randomization	Not relevant to our study. For Biochemical part: Measurements are usually normalized to the wild type situation to deduce if mutant proteins alter the activity of the examined protein.
Blinding	Not relevant to our study since cryo-EM and biochemical study of our sample required knowledge of included components and experimental setup.

Reporting for specific materials, systems and methods

Materials & experimental systems

n/a	Involved in the study
☐	☒ Unique biological materials
☐	☒ Antibodies
☒	☐ Eukaryotic cell lines
☒	☐ Palaeontology
☒	☐ Animals and other organisms
☒	☐ Human research participants

Methods

n/a	Involved in the study
☒	☐ ChIP-seq
☒	☐ Flow cytometry
☒	☐ MRI-based neuroimaging

Unique biological materials

Policy information about availability of materials

Obtaining unique materials	We derived fresh pig livers from the slaughterhouse to isolate mitochondria and subsequently mitochondrial ribosomes from them.

Antibodies

Antibodies used	anti-SBP-HRP antibodies (Santa Cruz, SB19-C4), Total OXPHOS Cocktail Antibody (ab110412) and β-actin (ab8226), IR Dye 800CW Goat Anti-Rabbit IgG or IR Dye 680LT Goat Anti-Mouse IgG (LI-COR) , bS16m antibody (Proteintech 16735-1-AP), mL45 antibody (Proteintech 16394-1-AP)
Validation	All antibodies have been described as suitable for quantitative immunoblot analysis on the manufacturer's websites.